

# Causal Longitudinal Image Synthesis

Yujia Li, Han Li, and S. Kevin Zhou, *Fellow, IEEE*,

**Abstract**—Clinical decision-making relies heavily on causal reasoning and longitudinal analysis. For example, for a patient with Alzheimer’s disease (AD), how will the brain grey matter atrophy in a year if intervened on the A-beta level in cerebrospinal fluid? The answer is fundamental to diagnosis and follow-up treatment. However, this kind of inquiry involves counterfactual medical images which can not be acquired by instrumental or correlation-based image synthesis models. Yet, such queries require counterfactual medical images, not obtainable through standard image synthesis models. Hence, a causal longitudinal image synthesis (CLIS) method, enabling the synthesis of such images, is highly valuable. However, building a CLIS model confronts three primary yet unmet challenges: mismatched dimensionality between high-dimensional images and low-dimensional tabular variables, inconsistent collection intervals of follow-up data, and inadequate causal modeling capability of existing causal graph methods for image data. In this paper, we established a tabular-visual causal graph (TVCG) for CLIS overcoming these challenges through a novel integration of generative imaging, continuous-time modeling, and structural causal models combined with a neural network. Specifically, we first depict the causality between tabular variables including demographic variables, clinical biomarkers, and brain volume size via a tabular-only causal graph (TOCG), and then further establish a tabular-visual causal graph (TVCG) to causally synthesize the brain MRI by developing an intervened MRI synthesis module (ISM) as an edge between TOCG and MRI. We train our CLIS based on the ADNI dataset and evaluate it on two other AD datasets, which illustrate the outstanding yet controllable quality of the synthesized images and the contributions of synthesized MRI to the characterization of AD progression, substantiating the reliability and utility in clinics.



## 1 INTRODUCTION

CLINICAL decision-making heavily depends on both **longitudinal** pattern comparison and **causal reasoning** [2], [5], [7], [86]. For instance, in clinical decision-making related to Alzheimer’s disease (AD), the most common type of dementia and a neurodegenerative disorder with a progression that can extend over decades [10]–[12], physicians initially assess changes in brain structure over time through longitudinal magnetic resonance image (MRI) scans [6]. They then integrate these changes with other tabular-variable factors, such as age and cognitive ability, drawing on their medical experience to understand the progression of AD. In this context, conducting longitudinal pattern comparison is relatively straightforward if longitudinal data are available, but integrating brain structure changes with other tabular-variable factors to understand the progression of AD poses a significant challenge. This difficulty arises because these factors are not impacted independently but are causally interrelated. Years of clinical experience in AD are essential for physicians to develop their own causal reasoning mechanism to understand AD progression.

However, even with high-quality longitudinal MRI and a robust causal reasoning mechanism, comprehending AD’s progression remains complex. This complexity largely stems from the need for physicians to consider specific ‘If’ questions to understand AD progression in fine granularity, such as: ‘If the patient were 10 years younger, how would their brain image appear?’ or ‘If there is an increase in the A-beta level in cerebrospinal fluid (CSF), how would it impact the grey matter volume (GMV)?’ These inquiries, known as *counterfactual* questions [6], [18], involve hypothesizing specific interventions that diverge from actual scenarios. As in Fig. 1, brain atrophy, a key clinical indicator in AD diagnosis, is influenced by numerous factors, including multiple covariates

and interventions. Typically, physicians compare brain size changes between MRI scans acquired say at  $t_1$  and  $t_2$ . They then attempt to answer counterfactual questions at different time points, like  $t_0$  or beyond  $t_2$ , based on the extrapolation of these changes and other factors. Subsequently, they determine the timing and nature of interventions needed to potentially slow down or reverse brain atrophy, which is indicated by the blue line in Fig. 1.

Addressing this issue ideally requires an imaging modality that can directly answer these counterfactual questions or assist physicians in understanding the causal mechanisms of AD. Unfortunately, no existing imaging modalities can meet this need. Consequently, a computational method, that generates novel longitudinal synthetic images while incorporating AD’s causal mechanisms and providing insights into counterfactual questions, emerges as a preferable solution. To this end, we hereby attempt to establish a tabular-visual causal graph (TVCG) for **causal longitudinal image synthesis** (CLIS) task that incorporates both causality and longitudinality, with a novel integration of causal graph [18] and generative imaging.

Specifically, we first depict the causality between longitudinal tabular variables including longitudinal demographic variables, clinical biomarkers, and brain volume size via a tabular-only causal graph (TOCG), and then further establish a tabular-visual causal graph (TVCG) by using an intervened MRI synthesis module (ISM) as an edge between longitudinal image and TOCG. This framework allows for the easy synthesis of counterfactual MRIs, addressing the aforementioned counterfactual questions through simple modifications of the variables (interventions) in TVCG.

When developing our TVCG, we encounter three primary yet unmet challenges: (1) *Mismatched dimensionality*: While the causal graph has demonstrated success in fields such as epidemiology, econometrics, and medicine [20]–

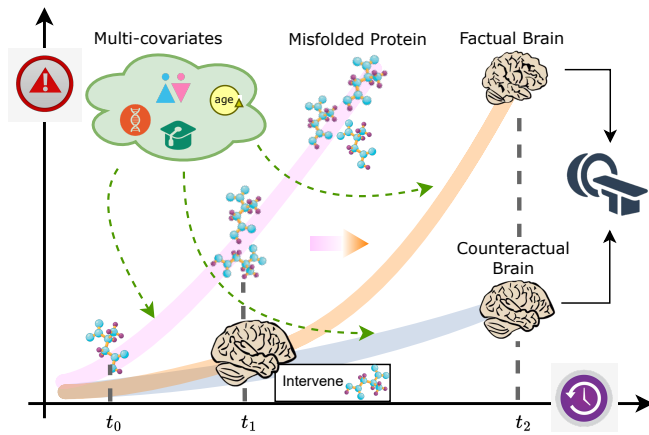


Fig. 1. The illustration of causal and longitudinal disease progression. Along the time axis, the accumulation of misfolded proteins has a causal effect on brain atrophy. Multiple covariates, including gene type, sex, education level, and baseline age, also have causal effects on the disease trajectories (shown in yellow). The blue trajectory represents the **counterfactual** brain atrophy when successfully intervened on the misfolded protein level at  $t_1$ , which deviates from the fact and results in a different MRI at  $t_2$ . We attempt to develop a computational model that leads to such a success.

[22], it primarily deals with low-dimensional tabular variables. In contrast, causal image synthesis involves both high-dimensional images and low-dimensional tabular variables. (2) *Inconsistent collection intervals* of training data: The most direct way to model AD progression is through training models with longitudinal data. Yet, the acquisition time of existing longitudinal MRI data varies from patient to patient, making it difficult to develop a model that can accommodate this variability. (3) *Inadequate causal modeling capability*: The causal mechanism of AD involves intricate interactions among various factors. Traditional causal graph methods, like Structural Causal Models (SCM), require pre-defined graph structures and often rely on linear causal relationship modeling (i.e., edge) [85], which can struggle to accurately represent these intricate relationships.

To address the challenge of *Mismatched dimensionality*, we propose the generative imaging method, ISM, as a feasible solution. The key idea of IMS is to represent a high-dimensional 3D medical volume with a medium-dimensional latent vector, which serves as a bridge between low-dimensional tabular variables and high-dimensional medical images. In ISM, we train a 3D StyleGAN [13] as a latent-to-image generator that defines a latent-to-image mapping function, and an accompanying neural network (NN) as an image-to-latent decoder that defines an image-to-latent mapping function. To address the challenge of *Inconsistent longitudinal collection intervals* of training data, we propose to incorporate the time interval as an independent variable in our model for the capability of continuous time prediction. Existing approaches tend to construct multiple models for a subset of discrete time points [44]–[46], which is not scalable and suffers from a scarcity of training data. To address the challenge of *Inadequate causal modeling capability* of traditional causal graph methods, our TVCG uses a Hybrid Causal Graph design, which merges Temporal Causal Graph (TCG) with Structural Causal Model (SCM)

techniques. This hybrid model incorporates TCG’s causal discovery mechanism and enhances it with SCM’s soft (deterministic or probabilistic) edge-fitting methods, thus leveraging the strengths of both methods. Moreover, during SCM edge-fitting, we use a neural network (NN) based approach. Compared with the commonly used linear edge representation in SCM, the NN edge representation demonstrates enhanced capability in modeling causal relationships compared to linear methods.

In summary, our key contributions are as follows.

- We propose a tabular-visual causal graph (TVCG) designed for the **causal longitudinal image synthesis (CLIS)** task. TVCG effectively tackles the three major challenges inherent in CLIS: the mismatched dimensionality of a high-dimensional image and low-dimensional tabular variables; inconsistent collection intervals of training data; and inadequate causal modeling capability of traditional causal graph methods.
- We evaluate our TVCG in both causality and longitudinal brain MRI synthesis tasks by several metrics. Our TVCG achieves the **best performances** compared with previous methods. Additionally, the synthesized images have also proven beneficial in a preliminary manner for predictive tasks such as the clinical characterization of AD.
- Beyond the image synthesis, TVCG shed light on the **causal relationships** among demographic, bio-markers, brain volume variables, and MR images. The causality is verified on external validation cohorts and may help to alleviate the spurious correlations for machine learning models.

## 2 RELATED WORK

### 2.0.1 Medical Image Synthesis

Medical image synthesis has a potential for mitigating challenges such as limited or absent data, privacy concerns, and dataset biases. Image synthesis across MRI, computed tomography (CT), and positron emission tomography (PET) [35]–[40] and among different MRI sequences [8], [42], [43], different resolutions [41], or the MRI’s of different categories (health or disease) [32], [33] have been widely explored.

However, limited research focuses on the prediction of medical images at future time-points because of the challenges of processing various session intervals and capturing the fine structure alternations among the scans for a single individual. LDGAN [46] and MI-GAN [45] predict multiple future data by training multiple models and are incapable of handling varying session intervals. Fan et al. [44] propose TR-GAN to deal with input sequences of varying lengths and generate future variant sessions, but it does not consider other modalities, such as bio-markers and demographic information.

There have been some attempts to introduce causality into medical image synthesis for multiple sclerosis [47], [48], brain tumor [49] and AD [93]. However, they concentrate on 2D images and lack effective metrics to evaluate the quality of synthesized images via causal intervention. They are also sectional and thus might be improper for downstream tasks.

### 2.0.2 Causal Model for Alzheimer's disease

Causal relationships in AD have been widely investigated in the fields of pathophysiology. The related factors include age [63]–[65], gender [68]–[70], education level [66], [67], risk genes [50]–[52], accumulated misfolded amyloid beta ( $A\beta$ ) and hyperphosphorylated tau protein ( $p\tau$ ) [53]–[56], grey matter loss [71]–[73], and enlarged ventricles [74], [75]. The current research exhibits a dual emphasis. The first group of methods concentrates on the interactions between two or three specific factors [78]–[84], while the others [87], [94] underscore the establishment of causal relationship networks among multiple factors, which is more related to our work.

Iturria-Medina et. al. [88] propose a multifactorial causal model to study the disease progression [89] and furthermore potential intervention. Shen et. al. [87] apply several causal discovery algorithms to AD to examine whether they can recover the causal graph from observational clinical data. Hu et. al. [94] collect prior causal knowledge and orient the arcs of a causal Bayesian network from diagnosed patient data. However, they either use extracted features of MRI or do not include MRI because of the intractability of the high-dimensional image data, which limits the modeling performance and clinical significance.

### 2.0.3 Characterization of Alzheimer's disease

A treatment given at an early stage of AD is more effective. Thus, a crucial task is to identify those at early disease stages, who are likely to progress over the short-to-medium term (1-5 years) [95] and may react positive to treatment. Thus, lots of research try to forecast early AD using some key features such as clinical status, cognitive decline, and brain atrophy.

There have been multiple works using various models, such as Gaussian process [97], recurrent neural network (RNN) [100], Bayesian latent variable model [98], and parametric model [99]. While all these models deal with the multi-modal data, the lack of future MRI restricts their performances; yet our method that is able to predict future MRI can alleviate this restriction.

The Alzheimer's Disease Prediction Of Longitudinal Evolution (TADPOLE) Challenge [96] compares the prediction performance of 58 algorithms. The participants train on historical data from the Alzheimer's Disease Neuroimaging Initiative (ADNI) [25] or other accessible datasets and are required to make monthly forecasts over a period of 5 years of total volume of the ventricles. We also apply our method to this part of the challenge and show better results.

## 3 PRELIMINARIES

To describe the causal relationships between time series, either Temporal Causal Graph (TCG) [19] or Structural Causal Model (SCM) [18] can be used. The edges in TCG can be dynamically modeled through training to indicate the presence or absence of causality between binary or continuous variables [3] in a **binary manner**. In contrast, in SCM, also known as Structural Equation Models (SEM), the presence or absence of each edge is predefined. These edges are then trained to represent causal relationships through either **deterministic or probabilistic** functions. In the following, we will introduce them, respectively.

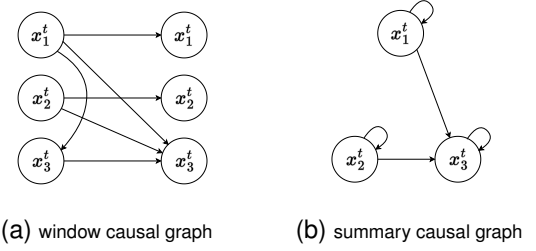


Fig. 2. An illustration of (a) a window causal graph of three variables in two-time steps. (b) the corresponding deduced summary causal graph.

### 3.1 Temporal Causal Graph (TCG)

We use a window causal graph, a special type of temporal causal graph, to introduce the mechanism of the causal relationships between the variables in TCG. A window causal graph  $\mathcal{G} = (\mathbf{V}, \mathbf{E})$  is a direct acyclic graph (DAG), defined as follows,

**Definition 1 (Window Causal Graph).**

Let  $\mathbf{x}$  be a  $d$  dimension variable which contains  $d$  components  $x_1, \dots, x_d$ . Each component (e.g.  $x_1$ ) contains a value to represent an attribute. In Window Causal Graph  $\mathcal{G} = (\mathbf{V}, \mathbf{E})$ , we got two sets: Node set  $\mathbf{V}$  and edge set  $\mathbf{E}$ . The node set  $\mathbf{V}$  contains various  $\mathbf{x}$  in different timestep  $t_0, t_1, \dots, t_\tau$ . Each  $\mathbf{x}$  still contains  $d$  components:

$$\mathbf{V} = [\mathbf{x}^1, \mathbf{x}^2, \dots, \mathbf{x}^t], \mathbf{x}^t = [x_1^t, x_2^t, \dots, x_d^t]. \quad (1)$$

As for the Edge set  $\mathbf{E}$ , we employ lag-specific DIRECTED links to interconnect different components, represented as  $x_i^{t_i} \rightarrow x_j^{t_j}$ ,  $x_i^{t_i} \neq x_j^{t_j}$ . These links can either be Forward-Cross-Time link ( $t_i < t_j$ ) or within-time link ( $t_i = t_j$ ). However, Reverse-Cross-Time link ( $t_i > t_j$ ) are not permitted. The difference  $t_j - t_i$  is termed as a time lag  $\tau$ .

Fig. 2a gives an illustration of a window causal graph. We set the window size as 1, hence the graph only focuses on two timesteps,  $t$  and  $t+1$ . This graph represents:  $x_1$  causes  $x_2$  with a time lag of 1,  $x_2$  causes  $x_3$  with a time lag of 1,  $x_1$  causes  $x_3$  with a time lag of both 0 and 1, and  $x_1, x_2, x_3$  all cause itself with a lag of 1. To be more concise, a simplified version of the window causal graph, termed as summary causal graph, is proposed to simplify the representation, which is shown in in Fig. 2b.

Subsequently, we use a summary causal graph as our representation.

**Definition 2 (Causal discovery).** Causal discovery refers to recovering a causal graph (TCG in this work) from observational data [4]. There have been multiple causal discovery methods, mainly including constraint-based [103], score-based [104], and functional-causal-models-based [105]. Most of the methods are designed based on multiple assumptions, primarily including the Causal Sufficiency and Faithfulness assumptions:

**Assumption 1 (Causal Sufficiency).** A set of variables is causally sufficient if all common causes of all variables are observed.

**Assumption 2 (Faithfulness).** A graph  $\mathcal{G}$  and a compatible probability distribution  $P$  are faithful to one another if

all and only the conditional independence relations true in  $P$  are entailed by the Markov condition applied to  $\mathcal{G}$ .

After the causal discovery is finished, an effective way to test its validness is Partial correlation analysis. Specifically, under the Causal Sufficiency and Faithfulness assumptions, for the observed variable set  $\mathcal{X} = \{x_1, x_2, \dots, x_N\}$

$$x_i \not\perp\!\!\!\perp x_j | \hat{\mathcal{X}} \iff x_i \leftrightarrow x_j \quad (2)$$

where  $\hat{\mathcal{X}} = \mathcal{X} \setminus \{x_i, x_j\}$ , i.e., the difference set resulting from subtracting  $\{x_i, x_j\}$  from  $\mathcal{X}$ , and  $x_i \leftrightarrow x_j$  means that there is a causal edge of unknown direction between  $x_i$  and  $x_j$ . A conditional independence test can be performed for the null hypothesis that the correlation is equal to zero.

### 3.2 Structural Causal Models

**Definition 3 (Structural Causal Model).** A structural causal model (SCM) is defined as

$$\mathcal{M} := \langle \mathcal{X}, \mathcal{U}, \mathbb{P}_{\mathcal{U}}, \mathcal{F} \rangle, \quad (3)$$

where

- 1)  $\mathcal{X}$  is a set of observed variables;
- 2)  $\mathcal{U}$  is a set of unobserved exogenous noise;
- 3)  $\mathbb{P}_{\mathcal{U}}$  is the distribution for  $\mathcal{U}$ ;
- 4)  $\mathcal{F}$  is  $\mathcal{X} \times \mathcal{U} \rightarrow \mathcal{X}$  is a measurable function that specifies the causal mechanism.

**Definition 4 (Structural equations).** Let  $\mathcal{M}$  be an SCM, the structural equations of the  $\mathcal{M}$  are the set of equations

$$x_i = f_i(\mathbf{x}_{pa_i}, u_i), x_i \in \mathcal{X}, u_i \in \mathcal{U}, \quad (4)$$

where  $\mathbf{x}_{pa_i}$  is the set of variables that have causal effect on  $x_i$ , i.e., the parent of  $x_i$ . The  $u_i$  is the unobserved exogenous noise associated with  $x_i$ .

TCG suffers from the limitation of only expressing the presence or absence of causal relationships, without accurately representing the magnitude and specific functions of causal effects. On the other hand, SCM can express specific causal relationships using various functions however the validity of the model is constrained by the rationality of the human-defined edges.

In this paper, our TVCG uses a Hybrid Causal Graph design, which merges TCG with SCM techniques. This hybrid model incorporates TCG’s causal discovery mechanism and enhances it with SCM’s soft (deterministic or probabilistic) edge-fitting methods, thus leveraging the strengths of both methods.

## 4 THE CLIS METHOD: TVCG

This section illustrates the proposed tabular-visual causal graph (TVCG) for the Causal Longitudinal Image Synthesis (CLIS) task. TVCG focuses on constructing a temporal causal graph model, which encompasses both tabular data and MRI, with the medical image serving as the target output. As shown in Fig. 3, there are two training processes: (1) **tabular-only causal graph (TOCG) establishment** and (2) **tabular-visual causal graph (TVCG) establishment**.

TABLE 1  
The definition of variables  $x_i$ .

variable	definition	unit
<b>demographic variables <math>\mathcal{S}</math></b>		
$x_1^t$	age at time $t$	years
$x_2^t$	biological gender: 0 for male and 1 for female	-
$x_3^t$	the duration of receiving education	years
$x_4^t$	the apolipoprotein E (APOE) gene (0/1/2)	-
<b>biomarker level <math>\mathcal{B}</math></b>		
$x_5^t$	the $A\beta_{1-42}$ level in cerebro-spinal fluid	pg/ml
$x_6^t$	the $\tau$ protein level in cerebro-spinal fluid	pg/ml
$x_7^t$	the $p\tau_{181}$ protein level in cerebro-spinal fluid	pg/ml
<b>brain and substructure volume <math>\mathcal{V}</math></b>		
$x_8^t$	the total intracranial volume (TIV)	ml
$x_9^t$	the ventricle volume (VV)	ml
$x_{10}^t$	the grey matter volume (GMV)	ml
<b>T<sub>1</sub>-weighted MR image data <math>\mathcal{X}</math></b>		
$x_{11}^t$	MR image cropped to $192 \times 192 \times 224$ with every voxel normalised to $[0, 1]$	mm <sup>3</sup>

In this section, we will first introduce the data we use, then detail the two training processes, and finally, describe TVCG’s intervened inference process for CLIS, and finally a downstream task to apply the prediction results of TVCG.

### 4.1 Data

To provide a clearer understanding of our TVCG, we use Alzheimer’s Disease (AD) as a working example, utilizing the widely used AD dataset, ADNI [25]. Balancing variable coverage and model complexity, we select 11 variables from the ADNI [25] dataset for our experiment, denoted as  $d = 11$ . For a better understanding, we list all these 11 variables in Table 1, and  $x_d^t$  represents the  $d$ -th observed variable at time  $t$  for an AD patient. Now, the union of them,  $\mathbf{x}$ , is a  $d$ -dimension variable:

$$\mathbf{x}^t = [x_1^t, \dots, x_d^t] = [\mathcal{S}^t, \mathcal{B}^t, \mathcal{V}^t, \mathcal{X}^t]. \quad (5)$$

Note that  $x_i$  can represent different data types; therefore, we further divide them into four distinct groups:  $\mathcal{S}$  for demographic variables,  $\mathcal{B}$  for bio-marker,  $\mathcal{V}$  for brain and substructure volumes, and  $\mathcal{X}$  for MRI. The total intracranial volume (TIV), ventricle volume (VV) and grey matter volume (GMV) are chosen as they are closely related to the AD progression [71]–[75].

### 4.2 Tabular-Only Causal Graph (TOCG) Establishment

Given the significant gap between tabular and image variables, we opt to first establish a TOCG  $\mathcal{G}[\mathcal{S}, \mathcal{B}, \mathcal{V}]$  instead of directly building the entire TVCG  $\mathcal{G}[\mathcal{S}, \mathcal{B}, \mathcal{V}, \mathcal{X}]$  for our CLIS. Specifically, there are two steps of the TOCG establishment: causal edge discovery, and structural causal model fitting, with the aid of pre-defined assumptions.

#### 4.2.1 Pre-defining Assumptions

Besides the Causal Sufficiency and Faithfulness assumptions defined in section 3.1, we further make the following three more assumptions based on the AD scenario.

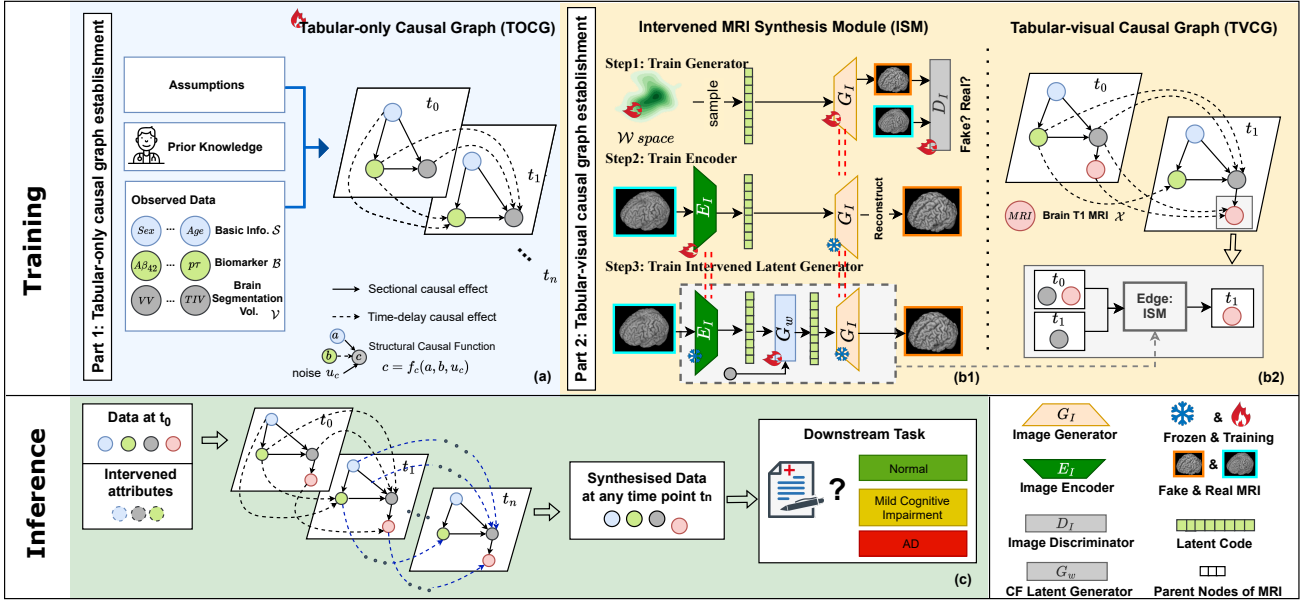


Fig. 3. The training and inference phases of the proposed tabular-visual causal graph (TVCG). The training includes two parts. (1) The tabular-only causal graph construction. Firstly causal discovery algorithms are applied to the observed tabular variables with assumptions and prior medical knowledge. Then for the recovered edges, the generative function is fitted. (2) The tabular-visual causal graph (TOCG) construction. An Intervened MRI Synthesis Module (ISM) is trained for the MRI generative. ISM is severed as an edge between tabular volume variables and MRI thus building TVCG over TOCG. The ISM training is a 3-step process: training an image generator, an image encoder, and an intervened latent generator. During inference, a set of baseline and optional intervention variables are input into the trained TVCG. The model computes the intervened tabular variables using the TOCG within TVCG, and the ISM generates the intervened MRI. These synthesized results are then applicable to downstream classification tasks.

**Assumption 3 (Markov Property).** The probability distribution of future states of  $\mathbf{x}$  depends only upon the present state, i.e.,

$$\forall \mathbf{x}, P(\mathbf{x}^t | \mathbf{x}^{t-1}, \dots, \mathbf{x}^1) = P(\mathbf{x}^t | \mathbf{x}^{t-1}), \quad (6)$$

which implies that there is no direct link when the time lag  $\tau$  is greater than 1.

**Assumption 4 (Self Temporal Causality).** There always exists a causal effect from  $\mathbf{x}_i^{t-1}$  on  $\mathbf{x}_i^t$ . i.e.,

$$\forall \mathbf{x}_i, \forall t, \mathbf{x}_i^{t-1} \xrightarrow{e} \mathbf{x}_i^t, \quad e \in \mathbf{E}, \quad (7)$$

where  $\mathbf{E}$  is the edge set of the causal graph and the only ‘exception’ is that for a constant factor, such as gender, there is no self-temporal causality.

**Assumption 5 (Prior Causal Hierarchy).** There is a causal hierarchy among different groups of variables, inspired from the prior knowledge [90]–[92]. Specifically,

(i) The demographic variables  $\mathcal{S}$  (e.g., gender) occupy the highest level: the edges from other modalities’ variables to demographic variables are prohibited:

$$\forall \mathbf{x}_i \notin \mathcal{S}, \forall \mathbf{x}_j \in \mathcal{S}, \mathbf{x}_i \xrightarrow{\hat{e}} \mathbf{x}_j, \quad \hat{e} \notin \mathbf{E}. \quad (8)$$

(ii) The biomarker variables  $\mathcal{B}$  (e.g., protein percentage) are with the second highest level: the edges from other modalities’ variables (except demographic) to biomarker variables are prohibited. i.e.,

$$\forall \mathbf{x}_i \notin (\mathcal{S} \cup \mathcal{B}), \forall \mathbf{x}_j \in \mathcal{B}, \mathbf{x}_i \xrightarrow{\hat{e}} \mathbf{x}_j, \quad \hat{e} \notin \mathbf{E}. \quad (9)$$

#### 4.2.2 Causal Edge Discovery

The causal edge discovery is used to model the presence of causal relationships as edges  $E$  in a causal graph. Specifically, by applying the Markov Property (Assumption 3), the causal discovery problem can be simplified to focus on the discovery of causal relationships with a maximum time lag of  $\tau_{max} = 1$ . Thus, for an observed trajectory  $\mathbf{x}^t$  with a time series length of  $T$ , the observational data can be arranged into pairs:

$$\mathbf{x}_{split} = \{(\mathbf{x}^1, \mathbf{x}^2), \dots, (\mathbf{x}^{T-1}, \mathbf{x}^T)\}, \quad (10)$$

where each  $(\mathbf{x}^{t-1}, \mathbf{x}^t)$  is an observational data pair from two consequence time steps ( $t-1$  and  $t$ ). Thus the causality discovery can be performed with the help of Assumptions 4 and 5.

Technically, we employ three widely used algorithms: FCI [103] (constraint-based), GES [104] (score-based), and DirectLiNGAM [105] (functional-causal-models-based). The results from these algorithms are integrated via a voting mechanism. The implementation leverages the Causal-learn package<sup>1</sup>, with several modifications made to the algorithms to comply with the constraints outlined in Assumptions 4 and 5. Detailed information on the algorithms is available in the code, and the validity of the learned causal model is discussed in the Experiments Section. The resulting causal graph is presented in Figure 4.

For testing conditional independence in the partial correlation analysis, as mentioned in Section 2, a  $t$ -test is utilized. We set the p-value threshold at 0.05 to reject the null hypothesis.

<sup>1</sup><https://github.com/py-why/causal-learn>

### 4.2.3 Structural Causal Model Fitting

After modeling the presence or absence of causal relationships (edges) via causal edge discovery, we further model these relationships (edges  $E$ ) via deterministic or probabilistic functions  $f$  as in SCM. In accordance with the TCG, the traditional SCM as Equ. (4) is extended to introduce time modeling interval  $\delta t$  for continuous-time as

$$x_i^{t_1} = f_i(\mathbf{x}_{pa_i}, u_i, \delta t), x_i \in \mathcal{X}, u_i \in \mathcal{U}, \quad (11)$$

where  $\mathbf{x}_{pa_i}$  is the set of variables that have causal effect on  $x_i$ .  $x_i^{t_1}$  is the variable  $i$  at time  $t_1$ .  $t_0$  is the time point of previous session and  $\delta t = t_1 - t_0$ .

We model the function  $f_i$  as a form of (1) Linear function, (2) Multi-layer Perceptron (MLP), or (3) Normalizing flow. Besides, we compare with Recurrent Neural Network (RNN) [100] and Long short-term memory (LSTM) [101], two bi-directional artificial neural networks that use an internal state to process arbitrary sequences. The details of the exact model of each function is provided in the supplementary.

Here we take MLP  $\hat{f}_{mlp}$  as an example. We assume an additive noise model [1] as

$$x_i^{t_1} = f_i(\mathbf{x}_{pa_i}, \delta t, u_i) := \hat{f}_{mlp}(\mathbf{x}_{pa_i}, \delta t) + u_i. \quad (12)$$

The **training objective function** is with  $L_2$  loss as

$$\mathcal{L} = \mathcal{L}_2(x_i^{t_1}, \hat{f}_{mlp}(\mathbf{x}_{pa_i}, \delta t)), \quad (13)$$

where  $x_i^{t_1}$  is the observation data.

### 4.3 Tabular-Visual Causal Graph (TVCG) Establishment

In this paper, we aim to process a variety of variables, including both tabular data  $\{\mathcal{S}, \mathcal{B}, \mathcal{V}\}$  and MRI  $\{\mathcal{X}\}$ . However, a TOCG is insufficient for this purpose, we still need to build a TVCG. A straightforward way to achieve this would be to treat MRI as a variable similar to the tabular variables. This presents a significant challenge due to the giant dimensional gap between tabular variables and MRI. In this paper, we propose to use an intervened MRI synthesis module (ISM) to bridge the gap.

Specifically, we first select three tabular variables that are directly associated with MRI from the established tabular-only causal graph. These variables are Total Intracranial Volume (TIV)  $x_8^t$ , Ventricular Volume (VV)  $x_9^t$ , Gray Matter Volume (GMV)  $x_{10}^t$ . Then our ISM modifies the MRI in the former time steps to synthesize a new MRI in the current time step according to the three variables. In this way, the ISM serves as an edge between the tabular-only causal graph and MRI data  $x_{11}^t$ , thereby realizing the TVCG.

In the following, we will first introduce the training process of ISM and then detail how to get the final TVCG.

#### 4.3.1 Intervened MRI Synthesis Module (ISM)

As shown in Fig. 3, We train our ISM in three steps: (1) Train a latent-to-image generator that can map a latent space to image space, (2) Train an image-to-latent encoder to perform an inverse mapping from image space back to a latent space, and (3) Train a volume-variable-to-latent generator to generate latent code based on volume variables. After that, We can employ the trained latent code generator to transform

any volume variables  $\mathcal{V} = \{x_8^t, x_9^t, x_{10}^t\}$  into latent codes and then synthesize images based on the latent codes via the trained generator and encoder. When the volume variables are derived from our causal graph, the synthesized image becomes a **causally-synthesized** image. In the following, we will introduce each step.

**Step1:** Train the latent-to-image generator. Unlike typical natural image synthesis tasks, MRI data for training are often limited, making it challenging to directly train an image-latent-image model. To mitigate this issue, we train our generator and encoder separately. In this way, the latent-to-image generator can be effectively trained by sampling latent codes from a distribution, thereby overcoming the constraints of limited data availability.

A style-based generative adversarial network (StyleGAN) is trained as the latent-to-image generator for its astonishing quality of generated images [9], [13]. The StyleGAN generator  $f_{style}$  firstly maps a multi-dimensional Gaussian distribution  $\mathcal{Z}$  to the latent space  $\mathcal{W}$  by a mapping network  $f_{map}$ :

$$f_{map} : \mathcal{Z} \rightarrow \mathcal{W}, \mathcal{Z} \subseteq \mathbb{R}^{128}, \mathcal{W} \subseteq \mathbb{R}^{128}, \quad (14)$$

and then a series of styled convolution blocks generate images  $\mathbf{I}$  from the sampled latent variable  $\mathbf{w}$  with Gaussian noise  $\mathbf{n}$  added:

$$\mathbf{I} = \mathbf{G}_{\mathbf{I}}(\mathbf{w}, \mathbf{n}), \mathbf{I} \in \mathbb{R}^{192 \times 224 \times 192}, \mathbf{w} \sim \mathcal{W}, \quad (15)$$

where  $\mathbf{G}_{\mathbf{I}}$  represents the styled convolution blocks.

A CNN discriminator  $\mathbf{D}_{\mathbf{I}}$  evaluates the synthesized image distribution and try to distinguish it from the true data distribution. The generator and discriminator are trained simultaneously but independently in an adversary way.

The **training objective functions** of discriminator  $\mathbf{D}_{\mathbf{I}}$  and generator  $\mathbf{G}_{\mathbf{I}}$  are given by

$$\begin{aligned} \mathcal{L}(\mathbf{D}_{\mathbf{I}}) &= \mathbb{E}_{\mathbf{w} \sim \mathcal{W}}[\mathbf{D}_{\mathbf{I}}(\mathbf{G}_{\mathbf{I}}(\mathbf{w}, \mathbf{n}))] - \mathbb{E}_{\mathbf{I} \sim data}[\mathbf{D}_{\mathbf{I}}(\mathbf{I})] \\ &\quad + \lambda_{grad} \mathbf{E}_{\mathbf{I}}[\|\langle \nabla \mathbf{D}_{\mathbf{I}}, \mathbf{I} \rangle\| - 1]^2, \end{aligned} \quad (16)$$

$$\mathcal{L}(\mathbf{G}_{\mathbf{I}}) = -\mathbb{E}_{\mathbf{w} \sim \mathcal{W}}[\mathbf{D}_{\mathbf{I}}(\mathbf{G}_{\mathbf{I}}(\mathbf{w}, \mathbf{n}))], \quad (17)$$

where the first and second terms in Equ. (16) represent the discriminator output expectation of generated and real distributions respectively. The third term is the Gradient Penalty.

**Step2:** Train the image-to-latent encoder. After we get a well-trained latent-to-image generator based on the Gaussian distribution, we now train an image-to-latent encoder to map the MRI to the latent code. In this way, we can modify the MRI (or intervene) by introducing the three variables into the latent code and synthesis the new MRI (or intervened MRI).

Specifically, with the well-trained StyleGAN as a fixed generator, an encoder  $\mathbf{E}_{\mathbf{w}}$  is trained to project MRI  $\mathbf{I}$  into the latent space  $\hat{\mathbf{w}}$ :

$$\hat{\mathbf{w}} = \mathbf{E}_{\mathbf{w}}(\mathbf{I}), \hat{\mathbf{w}} \in \mathcal{W}^* \subseteq \mathbb{R}^{12 \times 128} \quad (18)$$

where  $\hat{\mathbf{w}}$  is the mapping latent code, laying in the  $\mathcal{W}^*$  space, which should align with the latent code space  $\mathcal{W}$  in the fixed styleGAN. It is worth noting that the latent code  $\mathbf{w} \in \mathcal{W} \subseteq \mathbb{R}^{128}$  only have 128 dimension, they are duplicated 12 times to fit the input the generator, while  $\mathcal{W}^* \subseteq \mathbb{R}^{12 \times 128}$  owns more

expressiveness, i.e., the cardinality of set  $\mathcal{W}$  is greater than  $\mathcal{W}^*$ :  $|\mathcal{W}| < |\mathcal{W}^*|$ . Tov et al's work [17] and supplementary material provide more information about space  $\mathcal{W}^*$ .

Our encoder is based on a backbone with a feature pyramid that generates three levels of feature maps [16]. The details of the encoder can be found in the supplementary material.

The **training objective functions** of image encoder  $\mathbf{E}_w$  and latent code discriminator  $\mathbf{D}_w$  are given by

$$\begin{aligned} \mathcal{L}(\mathbf{E}_w) = & \mathcal{L}_1(\mathbf{G}(\mathbf{E}_w(\mathbf{I}), \mathbf{n}), \mathbf{I}) \\ & + \lambda_{freq} \mathcal{L}_1(\mathcal{F}(\mathbf{G}(\mathbf{E}_w(\mathbf{I}), \mathbf{n})), \mathcal{F}(\mathbf{I})) \\ & - \lambda_{ad} \mathbb{E}_{\mathbf{I} \sim data} [\mathbf{D}_w(\mathbf{E}_w(\mathbf{I}))] \\ & + \lambda_{reg} \mathcal{L}_{reg}(\mathbf{E}_w(\mathbf{I})), \end{aligned} \quad (19)$$

$$\begin{aligned} \mathcal{L}(\mathbf{D}_w) = & \mathbb{E}_{\mathbf{I} \sim data} [\mathbf{D}_w(\mathbf{E}_w(\mathbf{I}))] - \mathbb{E}_{w \sim \mathcal{W}} [\mathbf{D}_w(w)] \\ & + \lambda_{grad} \mathbf{E}_w \mathcal{W} [\|(\nabla \mathbf{D}_w)w\| - 1]^2. \end{aligned} \quad (20)$$

where the L1 loss in both the image domain and frequency domain ( $\mathcal{F}$ : Fourier Transform) enables learning on a pixel-wise basis while also avoiding blurry images that result from the loss of important frequencies. A regularisation term and a latent discriminator trained adversarially is applied to restrict  $\mathcal{W}^*$  not to deviate from  $\mathcal{W}$  too far.

For an MRI, the trained encoder projects it to the latent space, and the Gaussian noise added to the image generator is obtained by optimizing

$$\hat{\mathbf{n}} = \arg \min_{\mathbf{n}} \mathcal{L}_1(\mathbf{I}, \mathbf{G}_I(\mathbf{E}_w(\mathbf{I}), \mathbf{n})). \quad (21)$$

**Step3: Train the intervened latent generator.** As mentioned in step 2, we want to introduce the three variables  $V$  into the latent code to synthesize the new MRI (or intervened MRI). However, the variables have different shapes from our latent code. Hence, a V-to-latent generator is trained to generate latent variables based on  $V$ , i.e., *brain and substructure volumes*. We term it as an Intervened latent generator since the three variables  $V$  are a kind of intervention to modify the MRI in the former timestep to get a new MRI.

Specifically, we use a lightweight 5-layer MLP as the Intervened latent generator. This design avoids the overfitting issue for the low-dimensional latent space. If a patient has undergone MRI at  $T$  different time steps  $T = [t_1, \dots, t_T]$ , the training objective function of the Intervened latent code generator  $\mathbf{G}_w$  is given by:

$$\begin{aligned} \mathcal{L}(\mathbf{G}_w) = & \sum_{t_n \in T} \sum_{t_m \in T} \mathcal{L}_1(\hat{w}^{t_n}, w^{t_n}(t_m)), t_m < t_n \\ w^{t_n}(t_m) = & \mathbf{G}_w(\hat{w}^{t_m}, \mathbf{V}^{t_m}, \mathbf{V}^{t_n}), \\ \hat{w}^{t_m} = & E_w(\mathbf{I}^{t_m}), \hat{w}^{t_n} = E_w(\mathbf{I}^{t_n}), \end{aligned} \quad (22)$$

where  $\hat{w}^{t_m}$  and  $\hat{w}^{t_n}$  denotes the mapping latent code of the MRI at time points  $t_m$  and  $t_n$ , respectively, projected by the trained encoder  $\mathbf{E}_w$ .  $w^{t_n}(t_m)$  is the output of  $\mathbf{G}_w$ . We train  $\mathbf{G}_w$  to approximate  $w^{t_n}(t_m)$  to the GT  $\hat{w}^{t_n}$ .

Likewise,  $\mathbf{V}^{t_n} = \{x_8^{t_n}, x_9^{t_n}, x_{10}^{t_n}\}$  and  $\mathbf{V}^{t_m} = \{x_8^{t_m}, x_9^{t_m}, x_{10}^{t_m}\}$  denotes the corresponding segmented brain volumes at visit time point  $t_n$  and  $t_m$ . In our case,  $t_m < t_n$ , which means  $\mathbf{G}_w$  are trained to transfer the former timestep MRI's latent code  $\hat{w}^{t_m}$  to the latter timestep

MRI's latent code  $\hat{w}^{t_n}$  conditioned in the modification  $\mathbf{V}_j^{t_m} \rightarrow \mathbf{V}_j^{t_n}$ .

During training, for a patient with  $T$  scans in total, we randomly select two scans  $t_n$  and  $t_m$  in each training epoch.

#### 4.3.2 TVCG Based on ISM

After we trained the ISM, we can directly add the MRI into the TOCG by treating ISM as an edge between the three volume variables and MRI.

Specifically, the three tabular volume variables  $V$ : TIV( $x_8$ ), VV( $x_9$ ), GMV( $x_{10}$ ) serve as the parent nodes (higher level variables) of the MRI  $X = \{I\} = \{x_{11}\}$ , the edges between them exactly define the trained ISM.

$$\begin{aligned} \mathcal{G}[\mathcal{S}, \mathcal{B}, \mathcal{V}] + \mathcal{X} & \xrightarrow{e=ISM} \mathcal{G}[\mathcal{S}, \mathcal{B}, \mathcal{V}, \mathcal{X}], ISM \in E \\ \mathcal{X}^{t+1} = \{x_{11}^{t+1}\} & = ISM(\mathcal{V}^t, \mathcal{V}^{t+1}, \mathcal{X}^t), \\ \mathcal{V}^t = \{x_8^t, x_9^t, x_{10}^t\}, & \mathcal{X}^t = \{I^t\} = \{x_{11}^t\}. \end{aligned} \quad (23)$$

Now we obtain the TVCG  $\mathcal{G}[\mathcal{S}, \mathcal{B}, \mathcal{V}, \mathcal{X}]$  and any modification over the node of the graph (e.g, over  $\mathcal{S}$  and  $\mathcal{B}$ ) causally affects the  $\mathcal{V}$  and further influences  $\mathcal{X}$ . The influence in  $\mathcal{X}$  caused by the graph is termed as an intervention in our work.

#### 4.4 Intervened Inference Processes

With the TVCG, we can address various counterfactual 'if' scenarios. These scenarios are categorized into two types based on their underlying hypotheses: 1) Questions related to MRI based on the brain volume hypothesis, and 2) Questions based on other hypotheses. For the first type, we directly synthesize the Intervened MRI using the ISM. For other hypothesis-based questions, the approach varies: if they pertain to tabular variables, we find answers using our TOCG; if they relate to MRI, we first estimate the corresponding brain volume via TOCG and then synthesis the Intervened MRI using ISM. In this part, we introduce the inference process of ISM and TVCG, respectively. We set the time interval as 1 during inference.

##### 4.4.1 ISM Inference for Brain Volume Hypothesis

In ISM, any intervention (or hypothesis) on volume variables  $\mathbf{V}^{t_m} \rightarrow \mathbf{V}^{t_n}$  results in a corresponding intervention in the MRI  $\mathbf{I}^{t_m} \rightarrow \mathbf{I}^{t_n}$ ,

$$\mathcal{X}^{t_n} = \{\mathbf{I}_{ism}^{t_n}\} = \mathbf{G}_I(\mathbf{G}_w(\mathbf{E}_w(\mathbf{I}^{t_m}), \mathbf{V}^{t_m}, \mathbf{V}^{t_n}), \hat{\mathbf{n}}), \quad (24)$$

where  $\mathbf{I}^{t_m}$  is the MRI at  $t_m$  and  $\mathbf{I}_{ism}^{t_n}$  is the synthesized MRI at  $t_n$ . In fact, ISM focuses on the difference between  $\mathbf{V}^{t_m}$  and  $\mathbf{V}^{t_n}$ , and synthesises  $\mathbf{I}_{ism}^{t_n}$  on the base of  $\mathbf{I}^{t_m}$ .

##### 4.4.2 TVCG Inference for Other Hypotheses

In our TVCG, any intervention on  $\mathcal{S}$ - or  $\mathcal{B}$ -variable causally leads to the change of other  $\mathcal{V}$  variables:  $\mathbf{V}^{t_m} \rightarrow \mathbf{V}^{t_n}$ . The  $\mathcal{V}^{t_n}$  are predicted first based on TOCG and then MRI  $\mathcal{X}^{t+1}$  is synthesized via ISM.

$$\{\mathcal{S}^{t_n}, \mathcal{B}^{t_n}, \mathcal{V}^{t_n}\} = \mathcal{G}[\mathcal{S}^{t_m}, \mathcal{B}^{t_m}, \mathcal{V}^{t_m}], \quad (25)$$

$$\mathcal{X}^{t_n} = \{\mathbf{I}_{ism}^{t_n}\} = ISM(\mathcal{V}_m^t, \mathcal{V}_n^t, \mathcal{X}_m^t). \quad (26)$$

Besides the longitudinal MRI counterfactual synthesis, TVCG can also answer the counterfactual question for tabular variables. For example, for a patient with AD, how will

be the brain grey matter atrophy in a year if intervened on the A-beta level in cerebrospinal fluid? The result is computed as

$$\begin{aligned} a &\rightarrow x_5^{t_m}, x_5 \in \mathcal{B}^{t_m} \\ \{\mathcal{S}^{t_n}, \mathcal{B}^{t_n}, \mathcal{V}^{t_n}\} &= \mathcal{G}[\mathcal{S}^{t_m}, \mathcal{B}^{t_m}, \mathcal{V}^{t_m}](x_5^{t_m}), \\ \Delta x_{10} &= x_{10}^{t_n} - x_{10}^{t_m}, x_{10}^{t_m} \in \mathcal{V}^{t_m}, x_{10}^{t_n} \in \mathcal{V}^{t_n}, \end{aligned} \quad (27)$$

where A-beta level( $x_5^t$ ) is set to  $a$  and  $\Delta x_{10}$  is the brain grey matter atrophy amount.

#### 4.5 Downstream Tasks

To demonstrate that the generated images possess clinical relevance in predicting the future progression of a patient’s condition, we employ the generated data to predict the patient’s diagnostic  $y^t$  classification as downstream tasks.

$$y^t = \begin{cases} 0 & \text{Normal Control;} \\ 1 & \text{Mild Cognitive Impairment;} \\ 2 & \text{AD.} \end{cases} \quad (28)$$

$$\hat{y}^t = F(\phi(\mathcal{X}^t), [\mathcal{S}^t, \mathcal{B}^t, \mathcal{V}^t]), \quad (29)$$

where  $\hat{y}^t$  is the predicted diagnosis class,  $\phi$  is a neural network (e.g., DenseNet121) to extract the image feature, and  $F$  is a classification network which takes in the extracted image feature and tabular variables  $x_j^t \in \{\mathcal{S}, \mathcal{B}, \mathcal{V}\}$ . We train the  $\phi$  and  $F$  jointly on real data.

$$\mathcal{L}(\phi, F) = l_{BCE}(y^t, F(\phi(\mathcal{X}^t), [\mathcal{S}^t, \mathcal{B}^t, \mathcal{V}^t])). \quad (30)$$

## 5 EXPERIMENTS

### 5.1 Datasets and Training Details

We train our models using the ADNI dataset (adni.loni.usc.edu), and to assess model generalization, we test them on two independent datasets: OASIS3 and NACC. Detailed information about these publicly available datasets is presented in Table 2. The ADNI dataset is our primary choice for model construction as it encompasses all variables listed in Table 1. The NACC dataset, lacking longitudinal data, and the OASIS dataset, missing biomarker variables and primarily comprising healthy individuals, is used for limited testing purposes. OASIS is specifically employed for evaluating the image-related components of our model, not for testing causality and downstream tasks. For imaging processing, all T<sub>1</sub> images are skull-stripped using ROBEX [106], aligned to the MNI152 space, resampled to 1mm isotropic resolution using ANTs [107], cropped to dimensions of 192×224×192, and normalized in voxel values to the range [0, 1]. We segment the processed MRI to obtain grey matter volume with ANTs and ventricle volume through a CNN segmentation model [108].

For the learning of MLP, NF, LSTM and RNN in Section 4.2.3, Adam is used with a learning rate of 0.001 and  $(\beta_1, \beta_2) = (0.9, 0.99)$ . All models are trained for 5,000 epochs.

In Section 4.3.1, we detail the progressive training approach for StyleGAN, starting with low-resolution images and progressively doubling the resolution at each phase.

TABLE 2  
The Basic Information of Three Datasets

ADNI			
Category	NC	MCI	AD
# of subjects	739	981	383
# of sessions	2675	3388	1570
Sex (Female/Male)	327/412	580/401	219/164
APOE (0/1/2)	516/202/21	493/379/109	123/181/79
Age at baseline	73.14(±6.23)	72.77(±7.54)	74.83(±7.90)
Years of education	16.54(±2.56)	15.99(±2.74)	15.28(±2.91)
NACC			
Category	NC	MCI	AD
# of subjects	1682	484	667
# of sessions	3463	894	1179
Sex (Female/Male)	1030/652	228/256	297/370
APOE (0/1/2)	1047/540/50	251/166/44	257/264/94
Age at baseline	68.85(±10.15)	72.14(±9.01)	71.67(±9.34)
Years of education	16.16(±4.01)	15.92(±6.32)	15.55(±7.31)
OASIS			
Category	NC	MCI	AD
# of subjects	495	24	62
# of sessions	1267	61	161
Sex (Female/Male)	295/200	11/13	19/43
APOE (0/1/2)	252/129/20	12/10/0	25/26/5
Age at baseline	67.74(±8.67)	70.22(±7.76)	73.22(±6.85)
Years of education	16.08(±2.55)	14.71(±2.47)	15.79(±2.51)

Beginning at  $6 \times 7 \times 6$ , the process culminates in generating images of  $192 \times 224 \times 192$  at a 1mm isotropic resolution over six phases. Due to increasing memory demands, the minibatch size is adjusted through the phases as 2048, 2048, 1024, 256, 64, 24. Both the discriminator and generator are optimized using Adam with  $(\beta_1, \beta_2) = (0, 0.99)$ . Learning rates are set at 0.001 for phases 1-4, 0.015 for phase 5, and 0.002 for the final phase. Each phase involves training on 2,000,000 samples, except the last one, which uses 150,000 mini-batches. The  $\lambda_{grad}$  parameter in the discriminator’s loss equation (Equ. (16)) is fixed at 10.

The image encoder  $\mathbf{E}_w$  and latent code discriminator  $\mathbf{D}_w$  are trained independently but simultaneously, as in StyleGAN. For the encoder loss, Equ. (19), the  $\lambda_{ad}$  is 0.005,  $\lambda_{freq}$  is 0.5 and  $\lambda_{reg}$  is 0.0001. The  $\lambda_{grad}$  in  $w$  discriminator loss, Equ. (16), is 10. The Optimizer Adam is used with a learning rate of 0.00001 for  $\mathbf{E}_w$  and 0.00002 for  $\mathbf{D}_w$  and  $(\beta_1, \beta_2) = (0.9, 0.99)$  for both. The mini-bath size is 16 and the training comprises the iterations of 100,000 batches. The code for this study is publicly available<sup>2</sup>.

## 5.2 Results

### 5.2.1 Causal Graph and Structural Causal Model

**Causal edge validity:** As outlined in Section 4.2.2, we utilize multiple causal discovery methods on the ADNI dataset to verify causality relationships, which are then tested on the NACC dataset. For causal discovery, the ADNI data is split into adjacent session pairs.

In practical terms, the ADNI dataset is divided into a 4:1 ratio for training and validation sets. We apply three causal discovery methods, FCI, GES, and DirectLiNGAM, to the training set. Due to the absence of longitudinal data

<sup>2</sup><https://github.com/jessyblues/Causal-Longitudinal-Image-Synthesis.git>

TABLE 3  
The training and test sets for causal discovery.

		# Subject	# Data Pairs	Interval Years
Training	ADNI	364	560	$2.03_{\pm 1.21}$
Test	ADNI	91	147	$1.95_{\pm 1.19}$
Test	NACC	97	97	-

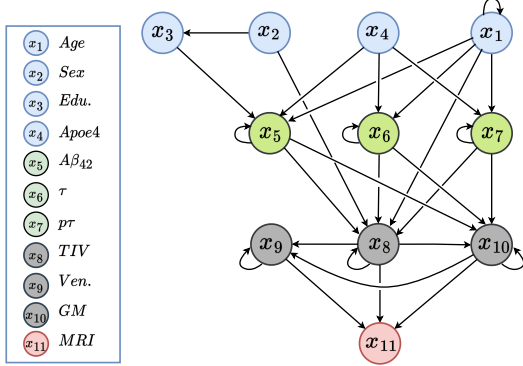


Fig. 4. The recovered causal graph, represented by a summary causal graph. Refer to Table 4 for a precise reference to each edge.

in NACC, we only test sectional causal relationships (causal edges with time lag 0) in this dataset.

Fig. 4 shows the recovered summary causal graph and Table 4 shows the recovered edges in detail. Overall, the introduction of prior knowledge 5 ensures that the causal relationships identified do not contradict common sense and existing research findings. For example, there exists no causal edge from  $t_1$  to  $t_0$ , which is contradicted by the time-priority assumptions, or causal edge from the brain tissue volumes to the bio-marker level, which is contradicted with the existing research, as the alternations of proteins is an early event in the progression of AD [90]–[92].

In the partial correlation analysis, 20 of the 25 identified edges demonstrate significance ( $\alpha > 0.05$ ) across the ADNI training set, ADNI validation set, and the NACC dataset. Figure 5 highlights the edges failing to meet this threshold, along with their respective t-test p-values. Five edges do not meet the criteria, with four (No.12, No.13, No.23, No.24) involving biomarker variables. Interestingly, these edges align with current clinical research. For instance, No.12 and No.13 suggest causal effects of age and the APOE gene on  $p\tau$  levels, both recognized as AD risk factors. No.21 indicates age’s impact on total intracranial volume (TIV), supported by references [60]–[62]. Also, No.23 and No.24 link  $\tau$  and  $p\tau$  levels to TIV, corroborated by [76], [77].

The  $t$ -test’s limited success might be attributed to biomarker value fluctuations due to varying measurement techniques. Despite normalization efforts, significant noise affects accuracy.

SCM fitting validity: This part includes assessing the predictive performance of fitted structural causal models. All available data pairs (not necessarily adjacent) are used for structural causal model fitting to capture both short and long-term interval relationships.

Our causality-based model, compared against leading time-series models, shows superior performance in pre-

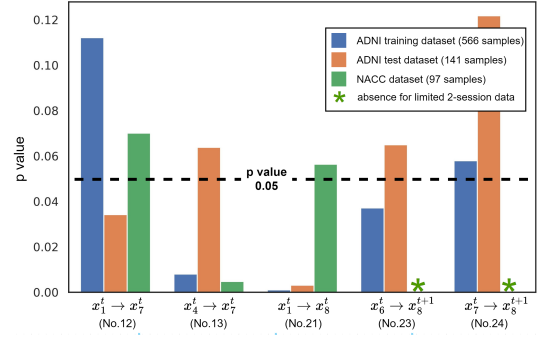


Fig. 5. The p-values of edges that do not meet the criteria of t-test in at least one dataset. Each sample of ADNI includes two adjacent session data as  $(\mathbf{X}^T, \mathbf{X}^{T+1})$ . The NACC dataset lacks multiple session data for a single subject thus only edges of instantaneous causality can be tested.

TABLE 4  
The recovered edges.

Self-Causality assumption			
$1.x_5^t \rightarrow x_5^{t+1}$	$2.x_6^t \rightarrow x_6^{t+1}$	$3.x_7^t \rightarrow x_7^{t+1}$	$4.x_8^t \rightarrow x_8^{t+1}$
$5.x_9^t \rightarrow x_9^{t+1}$	$6.x_{10}^t \rightarrow x_{10}^{t+1}$		
Recovered by all methods			
$7.x_2^t \rightarrow x_3^t$	$8.x_1^t \rightarrow x_5^t$	$9.x_4^t \rightarrow x_5^t$	$10.x_1^t \rightarrow x_6^t$
$11.x_4^t \rightarrow x_6^t$	$12.x_1^t \rightarrow x_7^t$	$13.x_4^t \rightarrow x_7^t$	$14.x_2^t \rightarrow x_8^t$
$15.x_1^t \rightarrow x_9^t$	$16.x_{10}^t \rightarrow x_9^t$	$17.x_8^t \rightarrow x_{10}^t$	$18.x_5^t \rightarrow x_{10}^{t+1}$
$19.x_6^t \rightarrow x_{10}^{t+1}$	$20.x_7^t \rightarrow x_{10}^{t+1}$		
Recovered by two methods			
$21.x_1^t \rightarrow x_8^t$ (FCI, GES)	$22.x_5^t \rightarrow x_8^{t+1}$ (FCI, GES)		
$23.x_6^t \rightarrow x_8^{t+1}$ (GES, LiNGAM)	$24.x_7^t \rightarrow x_8^{t+1}$ (GES, LiNGAM)		
$25.x_8^t \rightarrow x_9^t$ (FCI, GES)			

dicting brain volume changes, as depicted in Table 5. For segmented volumes (TIV, VV, and GMV), the data includes 2,762 sessions from 786 subjects (average interval:  $2.70_{\pm 2.47}$  years) and 688 sessions from 186 subjects (average interval:  $2.38_{\pm 2.17}$  years). However, due to limited CSF biomarker data, the training set for CSF biomarkers ( $A\beta$ ,  $\tau$ , and  $p\tau$ ) consists of 1,231 sessions from 382 subjects (average interval:  $3.38_{\pm 2.51}$  years), and the test set includes 318 sessions from 109 subjects (average interval:  $3.11_{\pm 2.13}$  years).

We utilize Normalized Mean Absolute Error (NMAE) as our metric, defined as  $NMAE = \frac{1}{N} \sum_{i=1}^N \frac{|y_i - \hat{y}_i|}{y_{max} - y_{min}}$ , where  $y_{max}$  and  $y_{min}$  are the maximum and minimum values of  $y$ ,  $y_i$  is the ground truth,  $\hat{y}_i$  the model prediction, and  $N$  the total number of test data.

We compare non-causality-based methods like non-causal linear models, MLPs, RNNs, and LSTMs, which use all variables to predict future outcomes, against causality-based approaches such as causal linear models, causal NFs, and causal MLPs, which only consider causal parent variables for predictions. In all cases except the  $A\beta$  variable, causality-based methods outperform their non-causal counterparts. The underperformance with  $A\beta$  may stem from its limited causal parent variables providing insufficient information. Notably, even the causal linear method rivals RNNs, LSTMs, and FC Networks in predicting  $p\tau$ , TIV, VV, and GMV, underscoring how causality enhances model robustness and mitigates spurious correlations.

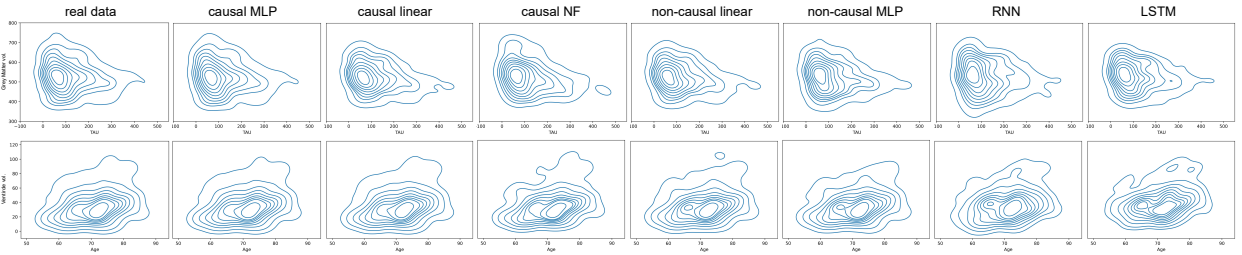


Fig. 6. The visualization of the data distribution predicted by different methods. The first row is the joint distribution of  $\tau$  (pg/ml) and grey matter volume (ml), while the second row is the joint distribution of age (years) and ventricle volume (ml). The first column is the distribution of real data and the second to eighth columns demonstrate the data distribution predicted by different methods. It appears that causal MLP performs the best.

TABLE 5  
The predicted non-image variables results of ADNI dataset.

Methods	NMAE↓					
	$A\beta$	$\tau$	$p\tau$	$TIV$	$VV$	$GMV$
Non-causal Linear	0.0664	0.0662	0.0552	0.0286	0.0273	0.0448
Non-causal MLP	0.0653	0.0578	0.0556	0.0197	0.0171	0.0366
RNN	<b>0.0480</b>	0.0577	0.0464	0.0333	0.0358	0.0568
LSTM	0.0488	0.0565	0.0506	0.0287	0.0276	0.0548
Causal Linear	0.0754	0.0720	0.0473	<b>0.0181</b>	0.0173	0.0378
Causal NF	0.0917	0.1008	0.0754	0.0292	0.0248	0.0581
Causal MLP	0.0518	<b>0.0553</b>	<b>0.0404</b>	0.0182	<b>0.0130</b>	<b>0.0326</b>

Figure 6 illustrates the data distributions from various methods. The first row shows the joint distribution of  $\tau$  and GMV, highlighting the negative correlation indicative of  $\tau$ 's toxicity and its causal effect on GMV atrophy, confirmed by research [57]–[59]. The second row's positive correlation between age and VV is aligned with findings in [60]–[62]. The causal MLP most accurately reflects the actual data distribution in both scenarios.

In summary, the causal MLP excels due to the neural network's superior modeling capabilities. However, the causal NF yields higher errors than the causal linear method in low-dimensional settings, suggesting its excessive complexity. This experiment validates our approach of integrating NNs with nonlinear complexity into SCM, effectively addressing **ineffective causal modeling**.

### 5.2.2 Causal Image Synthesis

For image synthesis, we utilize StyleGAN, known for its exceptional quality in generating natural images [13] and its popularity in image manipulation. We compare StyleGAN with AE-GAN (a variational autoencoder GAN) [112], wGAN (a classical Wasserstein GAN with gradient penalty) [113], and HA-GAN (a hierarchically-amortized GAN for 3D medical image synthesis) [114].

Quality of sampled MRI synthesis: To evaluate the quality of synthesized MRIs, we calculate the Fréchet Inception Distance (FID) and Maximum Mean Discrepancy (MMD), as shown in Table 6. Both metrics assess the divergence between image distributions, with lower values indicating more realistic MRI simulations. For FID, we use the middle slice from the Sagittal, Coronal, and Axial axes as 2D images and calculate their mean. MMD is computed from a stack of 8 slices.

Except for Latent Diffusion Models (LDM), all methods are trained on the ADNI dataset and tested for FID and

TABLE 6  
The performance comparison of sampled MRI quality.

Method	ADNI	OASIS	NACC	#params (Mb)	inf. time (S)
	FID <sub>i</sub> /MMD <sub>i</sub> ↓	FID <sub>i</sub> /MMD <sub>i</sub> ↓	FID <sub>i</sub> /MMD <sub>i</sub> ↓		
VAE-GAN	181.91 <sub>±0.57</sub> /6.60 <sub>±0.01</sub>	189.71 <sub>±0.72</sub> /6.91 <sub>±0.02</sub>	183.94 <sub>±0.80</sub> /6.78 <sub>±0.02</sub>	1739.68	0.088 <sub>±0.015</sub>
WGAN	167.90 <sub>±3.43</sub> /7.73 <sub>±0.02</sub>	177.14 <sub>±1.21</sub> /7.88 <sub>±0.02</sub>	182.35 <sub>±1.44</sub> /7.66 <sub>±0.03</sub>	481.49	0.094 <sub>±0.016</sub>
HA-GAN	62.69 <sub>±0.99</sub> /5.62 <sub>±0.01</sub>	80.85 <sub>±1.86</sub> /6.36 <sub>±0.03</sub>	69.27 <sub>±0.93</sub> /5.89 <sub>±0.01</sub>	304.20	0.177 <sub>±0.054</sub>
LDM	64.87 <sub>±0.64</sub> /6.13 <sub>±0.08</sub>	74.26 <sub>±1.67</sub> /6.55 <sub>±0.09</sub>	56.08 <sub>±0.34</sub> /6.24 <sub>±0.03</sub>	2162.68	7.612 <sub>±0.228</sub>
Ours	32.90 <sub>±0.36</sub> /3.27 <sub>±0.02</sub>	53.72 <sub>±0.44</sub> /3.90 <sub>±0.06</sub>	48.07 <sub>±0.41</sub> /3.33 <sub>±0.03</sub>	30.06	0.005 <sub>±0.007</sub>
real Data	7.90 <sub>±0.08</sub> /1.42 <sub>±0.06</sub>	19.53 <sub>±0.25</sub> /1.78 <sub>±0.07</sub>	10.46 <sub>±0.41</sub> /1.55 <sub>±0.02</sub>	-	-

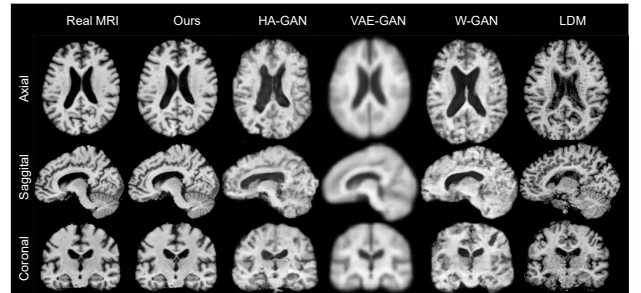


Fig. 7. The visualization of the MRI reconstructed by different methods. The first row, second row, and third row respectively show the axial, sagittal, and coronal slice. The first column demonstrates the real MRI and the second to five columns illustrate the MRI reconstructed by different methods.

MMD against real images from ADNI, OASIS, and NACC datasets. Due to computational constraints, we use a pre-trained LDM checkpoint by MONAI [109], [110], trained on the UK Biobank (UKB) dataset [111]. For fairness, we remove skulls from LDM output using ROBEX [106].

As Table 6 indicates, StyleGAN achieves the lowest FID and MMD values with fewer parameters and faster inference time. The higher FID and MMD for LDM may be due to dataset differences between UKB and ADNI. Additionally, LDM's slow inference and large parameter count hinder its use in our MRI synthesis module.

MRI reconstruction involves training an encoder to map MRIs to latent space. For W-GAN, HA-GAN, and LDM, we use a ResNet50-based encoder. LDM employs encoded MRI features to guide its denoising process, as described in []. VAE-GAN utilizes its integrated trained encoder. Our style-based generator's encoder is detailed in Section 4.3.1. As Fig. 7 demonstrates, only StyleGAN produces high-quality MRI reconstructions. VAE-GAN results are blurry, while w-GAN and HA-GAN introduce distortions. LDM reconstructions show substantial noise.

Quality of volume-intervened MRI synthesis: We test

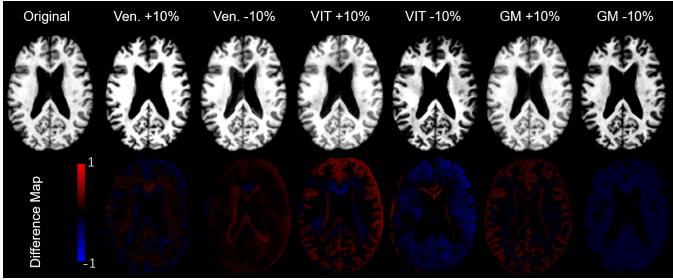


Fig. 8. The visualization of the synthesized MRI intervened on different volumes. The first row shows the axial slice of the MRI and the second row includes the corresponding difference map w.r.t. the original MRI in the first column.

the performance of ISM in generating brain MRIs that intervened on specific brain volumes, including VV, GMV, and TIV. Desired volume changes are set between +15% and -15%, and the intervened images are analyzed using ANTs [107] to confirm actual volume alterations. Table 7 presents the average and standard deviation of the actual volume changes, derived from the segmented volumes of the synthesized MRIs.

Fig. 9 features a Bland-Altman plot demonstrating the discrepancy between desired and actual volumes in the synthesized MRIs. The plot’s x-axis indicates the average of the desired and synthesized MRI volumes, while the y-axis shows their difference. Different datasets are denoted by varying dot types.

From Table 7 and Fig.9, it is evident that the ADNI-trained model can accurately synthesize MRIs with interventions across various datasets. The maximum error observed was a 3.27% deviation in MRI with a 15% increased ventricle volume on the OASIS dataset. The stability of outputs tends to decrease with larger desired changes, especially at the extremes of +15% and -15%. This trend is particularly noticeable for VV interventions, where errors grow as the original VV increases. The first row of Fig.9 illustrates this, showing a larger and more dispersed difference as the desired volume diverges from the original.

Fig. 8 displays visualizations of volume-intervened MRI. The difference map  $I_{diff} = I_{vt} - I_{ori}$  illustrates volume changes, with blue indicating decreased and red increased brain tissue intensity. For example, the second column shows a 10% ventricle enlargement, evidenced by blue around the ventricle. Interventions on total intracranial volume are demonstrated in the third and fourth columns, with red indicating tissue addition and blue indicating reduction, corresponding to the desired changes.

Longitudinal MRI synthesis: We evaluate our CLIS model’s performance in generating future session images with M12 (the 12-th month from baseline), M24 (the 24-th month from baseline), and M48 (the 48-th month from baseline) using ADNI and NACC datasets. Our method is compared against image translation methods Pix2Pix [115], CycleGAN [116], and MRI-specific networks MI-GAN [45], LD-GAN [46], and TR-GAN [44].

MI-GAN [45] is a Multi-Information GAN, which estimates brain MRI at future time-point conditioning on the brain MRI at baseline time-point and multiple information: gender, education level, and APOE gene. LD-GAN [46] is

TABLE 7  
The performance of volume intervention.

Dataset	Desired Change (%)	Actual Change		
		VV (%)	GMV(%)	TIV(%)
ADNI	-15	-17.54 $\pm$ 3.51	-15.01 $\pm$ 1.38	-13.44 $\pm$ 2.66
	-10	-11.39 $\pm$ 3.19	-9.32 $\pm$ 1.21	-9.24 $\pm$ 1.05
	-5	-5.95 $\pm$ 1.29	-4.31 $\pm$ 0.52	-5.36 $\pm$ 1.06
	5	6.28 $\pm$ 1.49	6.31 $\pm$ 1.05	6.08 $\pm$ 1.08
	10	11.38 $\pm$ 2.41	9.01 $\pm$ 1.61	8.12 $\pm$ 2.41
OASIS	15	17.51 $\pm$ 3.45	13.66 $\pm$ 1.74	12.81 $\pm$ 2.62
	-15	-13.88 $\pm$ 2.06	-14.02 $\pm$ 2.44	-13.97 $\pm$ 2.13
	-10	-12.71 $\pm$ 1.24	-12.98 $\pm$ 1.69	-11.80 $\pm$ 1.40
	-5	-5.73 $\pm$ 1.33	-5.19 $\pm$ 1.67	-5.11 $\pm$ 1.56
	5	4.43 $\pm$ 1.43	6.31 $\pm$ 1.63	5.43 $\pm$ 1.34
NACC	10	10.61 $\pm$ 1.73	11.99 $\pm$ 1.39	11.10 $\pm$ 1.85
	15	18.27 $\pm$ 2.46	14.26 $\pm$ 1.78	14.75 $\pm$ 1.99
	-15	-16.94 $\pm$ 2.37	-13.94 $\pm$ 2.24	-14.00 $\pm$ 2.49
	-10	-12.34 $\pm$ 2.34	-8.06 $\pm$ 2.02	-8.38 $\pm$ 1.64
	-5	-3.35 $\pm$ 1.99	-5.18 $\pm$ 1.73	-3.77 $\pm$ 1.47
	5	5.57 $\pm$ 1.30	4.02 $\pm$ 1.20	3.75 $\pm$ 2.08
	10	11.20 $\pm$ 2.58	9.21 $\pm$ 2.10	9.22 $\pm$ 2.22
	15	13.58 $\pm$ 3.43	14.36 $\pm$ 2.19	13.19 $\pm$ 2.66

a Longitudinal-Diagnostic GAN, which imputes MRIs by learning a bi-directional mapping between MRIs of two adjacent time points and performing clinical score prediction jointly, thereby explicitly encouraging task-oriented image synthesis. TR-GAN [44] is a Temporal Recurrent GAN to complete missing sessions of MRI datasets and adopts recurrent connections to deal with variant input sequence lengths and flexibly generate future sessions.

For generating the future M<sub>12</sub>, M<sub>24</sub> and M<sub>48</sub> images, our model only takes the baseline session and predicts all the multiple future sessions in a universal way, while the Pix2Pix, CycleGAN, and MI-GAN models cannot deal with the varying intervals so we train 3 models for them separately. The TR-GAN and LD-GAN models are designed for multiple inputs, however, for comparison fairness, the model also only takes the baseline session as input.

Quantitative results, including mean absolute error (MAE), multi-scale structural similarity (SSIM) index, and Peak Signal-to-Noise Ratio (PSNR), are detailed in Tables 8 and 9. The *t*-test is performed for significance analysis with \* for  $p < 0.05$ , \*\* for  $p < 0.01$ , and \*\*\* for  $p < 0.001$ . Our method consistently outperforms other models across metrics and datasets, particularly for M24 and M48 predictions, highlighting the significance of incorporating multi-session relationships.

Table 9 compares volumetric feature performance. Our model demonstrates the closest match to actual MRI volumes, indicating its superior accuracy in predicting VV, GMV, and TIV changes. The *t*-test is performed for significance analysis with \* for  $p < 0.05$ , \*\* for  $p < 0.01$ , and \*\*\* for  $p < 0.001$ . All models show increased errors on the NACC test dataset due to population differences, yet our model exhibits better generalization and less performance degradation.

As NACC only serves as a test dataset, and there exists a population shift compared with the ADNI training dataset; hence all models exhibit poorer performance on the NACC dataset, with larger errors in the volumes of generated MRI. However, compared with other methods,

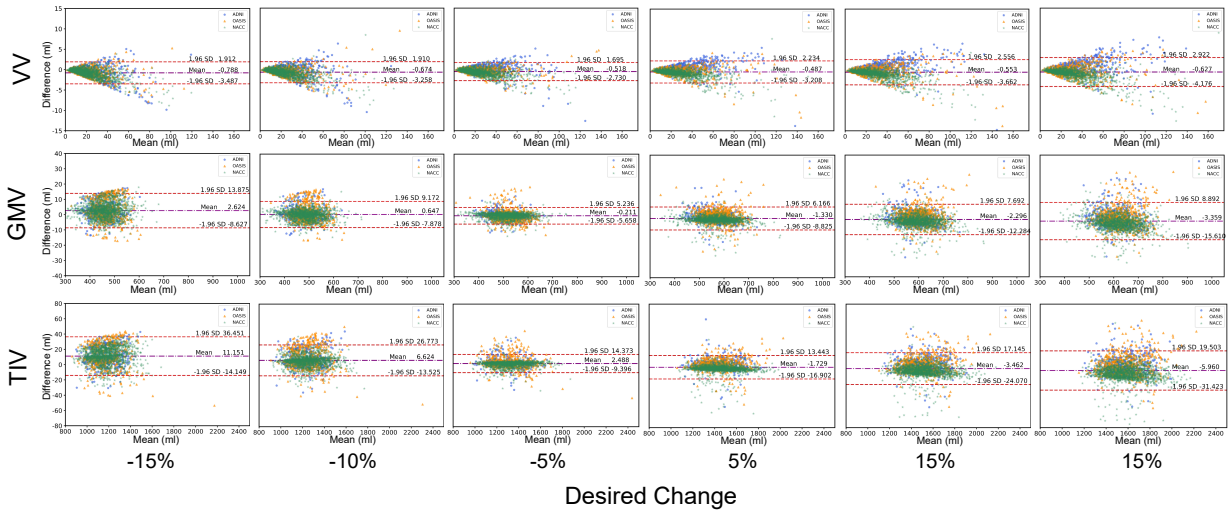


Fig. 9. The Bland-Altman plot to illustrate the disparity between the desired volumes and the synthesized MR volumes. The first row illustrates the VV, the second row illustrates the GMV and the third row illustrates the TIV. From left to right, the column represents the desired change percentage from -15% to 15%. In each sub-figure, the x-axis represents the mean value of the desired volume and the synthesized MR volume while the y-axis represents the difference between the desired volume and the synthesized MR volume.

TABLE 8

The quantitative performance of the longitudinally synthesized images.  $M_n$  denote the n-th month from baseline. e.g.,  $M_{00} \rightarrow M_{12}$  means the synthesis of MRI at 12-th month on the basis of the MRI at 0-th month.

Dataset	Method	$M_{00} \rightarrow M_{12}$ test:131/217 sub			$M_{00} \rightarrow M_{24}$ test:91/417 sub			$M_{00} \rightarrow M_{48}$ test:41/165 sub		
		MAE↓	SSIM(%)↑	PSNR(dB)↑	MAE↓	SSIM(%)↑	PSNR(dB)↑	MAE↓	SSIM(%)↑	PSNR(dB)↑
ADNI	Pix2Pix [115]	0.020±0.005***	94.9±1.7***	26.06±1.01***	0.023±0.006***	94.3±1.9***	25.61±1.79***	0.027±0.008***	92.9±2.8***	23.62±1.85***
	CycleGAN [116]	0.014±0.002***	95.9±0.7***	26.39±0.89***	0.019±0.003***	93.3±1.1***	25.76±1.02***	0.024±0.004***	90.8±1.4***	24.08±1.63***
	MI-GAN [45]	0.016±0.007***	95.4±0.6***	28.33±1.23***	0.043±0.006***	92.4±1.9***	19.02±1.66***	0.042±0.004***	92.2±0.9***	19.20±1.76***
	LD-GAN [46]	0.013±0.003***	97.5±0.7***	29.11±1.65***	0.015±0.003***	96.3±1.2***	28.27±1.74***	0.021±0.004***	95.5±1.2***	26.68±2.10***
	TR-GAN [44]	0.012±0.010***	97.1±4.3**	29.12±1.90***	0.012±0.008*	97.3±2.9*	29.05±1.48**	0.014±0.011*	96.8±3.4*	27.82±2.32***
	CLIS (ours)	<b>0.008±0.002</b>	<b>98.4±0.9</b>	<b>31.33±1.81</b>	<b>0.009±0.003</b>	<b>98.2±1.4</b>	<b>30.71±2.22</b>	<b>0.011±0.003</b>	<b>97.8±1.5</b>	<b>29.76±2.23</b>
NACC	Pix2Pix [115]	0.021±0.008***	94.3±3.2***	25.64±1.83***	0.025±0.008***	94.1±2.2***	24.85±2.67***	0.026±0.015***	92.7±2.9***	22.84±2.81***
	CycleGAN [116]	0.016±0.004***	95.3±1.8***	25.67±1.52***	0.022±0.004***	94.7±2.3***	25.29±2.08***	0.027±0.005***	91.8±2.8***	21.73±2.09***
	MI-GAN [45]	0.031±0.004***	92.9±1.3***	21.19±1.53***	0.044±0.008***	92.7±3.1***	18.39±1.67***	0.043±0.010***	92.2±4.3***	18.76±2.45***
	LD-GAN [46]	0.020±0.005***	95.8±1.9***	26.78±2.74***	0.022±0.003***	95.1±2.4***	26.23±2.72***	0.024±0.006***	94.0±3.1***	25.52±3.03***
	TR-GAN [44]	0.014±0.010***	96.2±4.8*	27.82±4.11***	0.013±0.005*	96.5±2.9*	27.84±2.73***	0.015±0.006**	95.6±3.4**	26.66±2.80***
	CLIS (ours)	<b>0.011±0.005</b>	<b>97.3±2.7</b>	<b>29.37±3.02</b>	<b>0.012±0.005</b>	<b>97.0±2.6</b>	<b>28.86±2.94</b>	<b>0.012±0.006</b>	<b>96.8±2.7</b>	<b>28.55±2.93</b>

our model demonstrates better generalization, with less performance degradation. As Table 9 shows, the largest performance degradation of our model happens in the  $M_{24}$  synthesis task, as the MAE of total intracranial volume increases from 13.99ml of ADNI to 21.53ml of NACC. On the other hand, while TR-GAN outputs the least error among the other methods, in terms of total intracranial volume, the gap between the MAE of TR-GAN and our model is 10.13/8.48/5.18 in ADNI for  $M_{12}/M_{24}/M_{48}$  MRI synthesis, the gap increases to 15.47/13.99/15.56 in NACC dataset, which confirms the better generalization of our model.

Fig. 10 presents the MRI visualization and error maps from different methods. Our method yields high-quality MRIs with few artifacts and blurs, closely matching the target MRI. In contrast, MI-GAN produces MRIs with inconsistent patches, while Pix2Pix and CycleGAN results are generally blurry. TR-GAN and LD-GAN exhibit incorrect tissue contrast, further highlighting the superior accuracy and generalization of our model.

### 5.2.3 Downstream Tasks of AD Characterization

To establish the clinical relevance of our generated images, we apply them to predict future disease progression in two tasks: AD classification and ventricle volume prediction.

Firstly, we conduct a three-class classification task (AD vs. NC vs. MCI) using ADNI and NACC datasets, with results presented in Table 10. We assess performance using multi-class AUC (mAUC), accuracy, F1 score, recall, and precision. The synthesized MRIs from our model prove comparable to real MRIs, surpassing other methods in almost all metrics across scenarios. Notably, our model demonstrates superior performance in the  $M_{48}$  task, the largest time interval, which is crucial yet challenging in clinical settings. The NACC dataset, having a higher proportion of NC cases, show that our model's advantage is less pronounced compared to ADNI.

Secondly, our method is applied in the TADPOLE Challenge for VV prediction, competing with 58 other algorithms. Our test set includes 696 sessions from 335 subjects, with an average interval of  $3.01 \pm 1.01$  years. Our model achieves an MAE of 0.39, outperforming the winning algo-

TABLE 9  
The performance comparison in terms of volumetric features.

Methods	Dataset	$M_{00} \rightarrow M_{12}$ test:131/217 sub			$M_{00} \rightarrow M_{24}$ test:91/417 sub			$M_{00} \rightarrow M_{48}$ test:41/165 sub		
		MAE of VV/ GMV / TIV (ml) ↓								
ADNI	Pix2Pix	5.63 $\pm$ 1.81***	25.36 $\pm$ 4.58***	23.76 $\pm$ 4.95***	5.94 $\pm$ 1.80***	29.32 $\pm$ 4.40***	25.25 $\pm$ 6.85***	7.28 $\pm$ 1.85***	46.44 $\pm$ 4.66***	26.17 $\pm$ 4.68***
	CycleGAN	8.35 $\pm$ 1.20***	24.05 $\pm$ 4.50***	31.09 $\pm$ 4.41***	9.92 $\pm$ 2.08***	24.03 $\pm$ 4.67***	28.52 $\pm$ 4.74***	10.22 $\pm$ 2.74***	37.69 $\pm$ 6.21***	30.67 $\pm$ 5.45***
	MI-GAN	2.74 $\pm$ 1.36**	22.75 $\pm$ 3.65***	50.51 $\pm$ 5.25***	4.76 $\pm$ 1.45***	86.20 $\pm$ 5.02***	67.20 $\pm$ 5.49***	6.51 $\pm$ 2.43***	76.95 $\pm$ 6.09***	67.92 $\pm$ 8.91***
	LD-GAN	3.38 $\pm$ 1.96***	28.41 $\pm$ 3.95***	30.68 $\pm$ 7.27***	3.33 $\pm$ 1.95*	43.75 $\pm$ 6.64***	43.02 $\pm$ 7.80***	6.37 $\pm$ 2.53***	46.95 $\pm$ 6.71***	32.16 $\pm$ 6.90***
	TR-GAN	3.01 $\pm$ 1.45***	14.48 $\pm$ 3.66*	23.90 $\pm$ 3.43***	3.26 $\pm$ 2.78*	16.94 $\pm$ 2.87*	22.47 $\pm$ 4.99***	4.38 $\pm$ 2.08*	23.34 $\pm$ 4.73*	23.21 $\pm$ 4.16***
	CLIS (ours)	2.27 $\pm$ 1.18	13.57 $\pm$ 2.34	13.77 $\pm$ 2.87	2.87 $\pm$ 1.14	16.28 $\pm$ 2.81	13.99 $\pm$ 2.54	3.63 $\pm$ 1.81	22.88 $\pm$ 2.27	18.03 $\pm$ 3.27
NACC	Pix2Pix	5.63 $\pm$ 1.67***	53.05 $\pm$ 5.15***	28.05 $\pm$ 2.31***	6.64 $\pm$ 1.98***	29.73 $\pm$ 4.00***	31.46 $\pm$ 5.53***	6.93 $\pm$ 2.23***	37.74 $\pm$ 4.45***	40.29 $\pm$ 6.58***
	CycleGAN	8.79 $\pm$ 1.88***	25.66 $\pm$ 5.51***	32.03 $\pm$ 6.99***	7.43 $\pm$ 1.97***	24.72 $\pm$ 4.49***	35.08 $\pm$ 8.29***	7.35 $\pm$ 2.31***	30.69 $\pm$ 4.83***	34.61 $\pm$ 9.28***
	MI-GAN	3.69 $\pm$ 5.33***	25.55 $\pm$ 2.31***	46.97 $\pm$ 2.16***	3.12 $\pm$ 2.81***	23.32 $\pm$ 2.24***	42.27 $\pm$ 4.89***	3.69 $\pm$ 5.33***	25.55 $\pm$ 2.31***	46.97 $\pm$ 2.16***
	LD-GAN	3.19 $\pm$ 1.76*	27.44 $\pm$ 3.65***	30.74 $\pm$ 7.15***	3.33 $\pm$ 1.95*	43.75 $\pm$ 6.64***	43.02 $\pm$ 7.80***	4.79 $\pm$ 2.70***	44.88 $\pm$ 6.35***	41.04 $\pm$ 8.68***
	TR-GAN	4.05 $\pm$ 1.69*	23.31 $\pm$ 1.79*	35.73 $\pm$ 3.01***	3.30 $\pm$ 2.54*	22.74 $\pm$ 2.12*	35.52 $\pm$ 2.75**	3.41 $\pm$ 3.19	30.30 $\pm$ 3.16**	38.75 $\pm$ 4.24***
	CLIS (ours)	2.43 $\pm$ 1.96	22.95 $\pm$ 2.37	20.26 $\pm$ 2.46	2.83 $\pm$ 1.54	21.99 $\pm$ 1.36	21.53 $\pm$ 3.35	3.28 $\pm$ 1.70	26.88 $\pm$ 1.49	23.19 $\pm$ 2.88

TABLE 10  
The performance comparison in terms of AD classification.

Methods	Dataset	$M_{00} \rightarrow M_{12}$ test:131/217 sub					$M_{00} \rightarrow M_{24}$ test:91/417 sub					$M_{00} \rightarrow M_{48}$ test:41/165 sub				
		mAUC / acc / F1 / recall / precision														
ADNI	Pix2Pix	0.916 / 0.782 / 0.594 / 0.648 / 0.553	0.833 / 0.769 / 0.566 / 0.617 / 0.526	0.769 / 0.700 / 0.508 / 0.558 / 0.473												
	CycleGAN	0.897 / 0.655 / 0.663 / 0.680 / 0.750	0.831 / 0.629 / 0.578 / 0.581 / 0.696	0.754 / 0.583 / 0.452 / 0.467 / 0.700												
	MI-GAN	0.797 / 0.660 / 0.492 / 0.576 / 0.438	0.613 / 0.538 / 0.392 / 0.469 / 0.389	0.527 / 0.411 / 0.276 / 0.379 / 0.317												
	LD-GAN	0.820 / 0.811 / 0.732 / 0.718 / 0.814	0.712 / 0.621 / 0.600 / 0.621 / 0.715	0.676 / 0.622 / 0.561 / 0.567 / 0.683												
	TR-GAN	0.913 / 0.785 / 0.608 / 0.654 / 0.888	0.848 / 0.769 / 0.566 / 0.617 / 0.526	0.805 / 0.700 / 0.508 / 0.558 / 0.473												
	CLIS (ours)	<b>0.926 / 0.881 / 0.848 / 0.826 / 0.906</b>	<b>0.865 / 0.804 / 0.727 / 0.712 / 0.810</b>	<b>0.825 / 0.717 / 0.573 / 0.592 / 0.813</b>												
NACC	Real Images	0.985 / 0.889 / 0.855 / 0.835 / 0.910	0.956 / 0.832 / 0.747 / 0.735 / 0.826	0.914 / 0.783 / 0.617 / 0.639 / 0.847												
	Pix2Pix	<b>0.865 / 0.802 / 0.779 / 0.772 / 0.805</b>	<b>0.878 / 0.883 / 0.802 / 0.754 / 0.881</b>	0.836 / 0.828 / 0.720 / 0.690 / 0.786												
	CycleGAN	0.857 / 0.763 / 0.725 / 0.704 / 0.814	0.865 / 0.847 / 0.744 / 0.685 / 0.857	0.809 / 0.816 / 0.692 / 0.651 / 0.769												
	MI-GAN	0.647 / 0.689 / 0.571 / 0.542 / 0.762	0.585 / 0.718 / 0.464 / 0.447 / 0.816	0.530 / 0.693 / 0.346 / 0.371 / 0.721												
	LD-GAN	0.856 / 0.809 / 0.788 / 0.783 / 0.812	0.804 / 0.809 / 0.788 / <b>0.783</b> / 0.812	0.797 / 0.833 / 0.732 / 0.715 / 0.791												
	TR-GAN	0.862 / 0.784 / 0.754 / 0.743 / 0.787	0.871 / 0.890 / 0.812 / 0.769 / <b>0.885</b>	0.825 / 0.828 / 0.724 / 0.701 / 0.786												
CLIS (ours)	0.863 / <b>0.813</b> / <b>0.792</b> / <b>0.785</b> / <b>0.816</b>	0.866 / <b>0.890</b> / <b>0.812</b> / 0.769 / <b>0.885</b>	<b>0.844 / 0.845 / 0.744 / 0.720 / 0.805</b>													
Real Images	0.881 / 0.831 / 0.808 / 0.799 / 0.837	0.900 / 0.911 / 0.833 / 0.785 / 0.913	0.847 / 0.885 / 0.779 / 0.739 / 0.854													

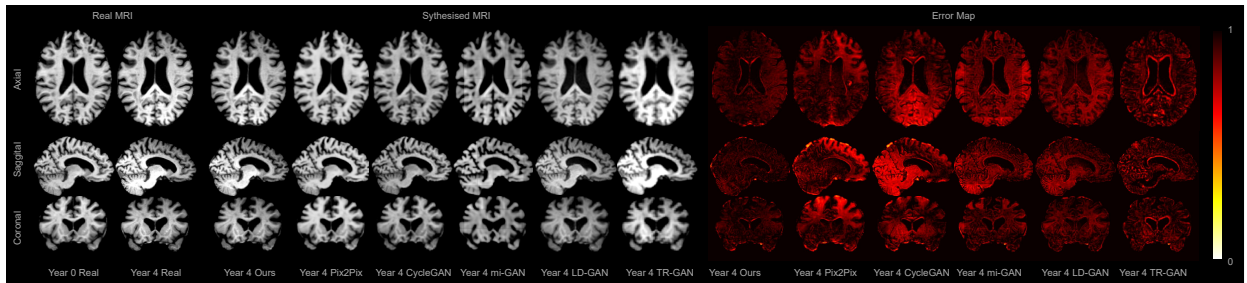


Fig. 10. The visualisation of the synthesized MRI by different methods. Based on the MRI at  $M_0$ , the methods synthesize MRI in  $M_{48}$  (4 years). Axial, sagittal, and coronal slices are displayed from the top row to the bottom. The error map represents the absolute error per voxel, on a scale from 0 to 1. In this map, higher values (indicated by brighter colors on the color bar) signify greater error.

rithm’s 0.41, without utilizing additional PET and DTI data available in the TADPOLE. We anticipate that incorporating PET and DTI data could further enhance our results.

#### 5.2.4 Counterfactual Questions

Our approach uniquely integrates a causality framework, enabling predictions in hypothetical scenarios and addressing the counterfactual question outlined in Section 1.

In these experiments, we intervene on the  $A\beta$  level in CSF or the age of the MCI group to predict counterfactual tabular variables and synthesize corresponding MRIs.

The MCI group is bifurcated into stable MCI (sMCI), who remain in the MCI stage, and progressive MCI (pMCI),

who progress to AD. Identifying subgroup affiliation is crucial for timely treatment. In the ADNI test set, we examine 50 MCI patients, including 33 pMCI and 17 sMCI, across 87 and 36 data sessions, respectively.

Figures 11b, 11c, and 11d illustrate predictions of GMV, VV, and TIV when intervening on  $A\beta$  levels in CSF for pMCI. Each individual is intervened to reach an  $A\beta$  level of 474.41 pg/ml, the sMCI mean in ADNI. Figure 11a reveals that most pMCI individuals have lower  $A\beta$  levels than this mean (the red line). This suggests that increasing  $A\beta$  in CSF may lead to larger GMV and TIV and smaller VV.

For counterfactual predictions, we use the same classifier as in Section 5.2.3. Of the 33 pMCI patients progressing

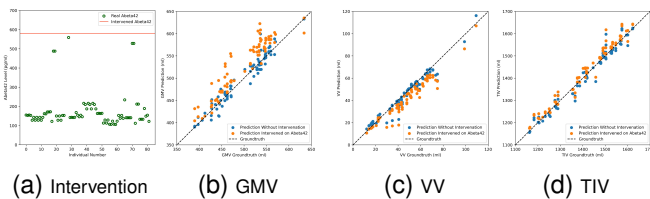


Fig. 11. The illustration of (a) the  $A\beta$  level in the subgroup pMCI and the intervened level (the mean level in sMCI) and the prediction of (b) GMV (c) VV, and (d) TIV with/without intervention of  $A\beta$  and the ground truth. The y-axis is the prediction and the x-axis is the according ground truth, thus a data point below the dashed line indicates a prediction higher than the ground truth, vice versa.

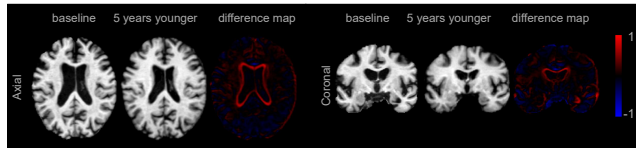


Fig. 12. The images display the MRI of a pMCI patient at the MCI stage alongside a synthesized MRI created by intervening on the age to appear five years younger. The first row presents the coronal slice, and the second row depicts the axial slice.

to AD, 24 are correctly identified as pMCI using factual synthesized MRI. However, this number drops to 15 with counterfactual MRI intervened at the  $A\beta$  level, suggesting that such interventions might slow AD progression. However, this insight is preliminary and requires clinical validation.

Figure 12 illustrates how a pMCI patient’s brain image might look if they were five years younger. We compute the difference map as  $I_{diff} = I_{intervened} - I_{original}$ , and the counterfactual MRI reveals a smaller ventricle and greater grey matter retention, aligning with current research [60]–[62], [82]. This approach can provide insights into past brain atrophy rates and assist clinicians in future progression predictions.

## 6 CONCLUSION

In this paper, we introduce the Tabular-Visual Causal Graph (TVCG) model for the Causal Longitudinal Image Synthesis (CLIS) task. By integrating causality and longitudinal analysis into image synthesis, TVCG avoids spurious correlations and surpasses previous methods in performance. Besides, the synthesized images of TVCG also show significant promise in clinical AD characterization.

A limitation of our model is the lack of modalities like PET and DTI, which could provide additional, crucial information that are not available in T1 MRIs. Future work should explore incorporating these modalities and examining their causal relationships. Additionally, our data-driven causal model building necessitates large datasets, so finding a more data-efficient construction approach is a key area for future research. All these further endeavors will guide us in evaluating CLIS’s practicality in real-world clinical contexts, encompassing AD and various other potential applications.

## REFERENCES

- [1] J. Peters *et al.*, “Causal inference on discrete data using additive noise models,” *IEEE Trans. Pattern Anal. Mach. Intell.*, vol. 33, no. 12, pp. 2436–2450, 2011.
- [2] J. Lin *et al.*, “Towards causality-aware inferring: A sequential discriminative approach for medical diagnosis,” *IEEE Trans. Pattern Anal. Mach. Intell.*, vol. 45, no. 11, pp. 13363–13375, 2023.
- [3] K. Olesen, “Causal probabilistic networks with both discrete and continuous variables,” *IEEE Trans. Pattern Anal. Mach. Intell.*, vol. 15, no. 3, pp. 275–279, 1993.
- [4] K. Li *et al.*, “Prediction of human activity by discovering temporal sequence patterns,” *IEEE Trans. Pattern Anal. Mach. Intell.*, vol. 36, no. 8, pp. 1644–1657, 2014.
- [5] C. A. Kulikowski, “Artificial intelligence methods and systems for medical consultation,” *IEEE Trans. Pattern Anal. Mach. Intell.*, vol. PAMI-2, no. 5, pp. 464–476, 1980.
- [6] K. Oh *et al.*, “Learn-explain-reinforce: Counterfactual reasoning and its guidance to reinforce an alzheimer’s disease diagnosis model,” *IEEE Trans. Pattern Anal. Mach. Intell.*, vol. 45, no. 4, pp. 4843–4857, 2023.
- [7] M. Ben-Bassat *et al.*, “Pattern-based interactive diagnosis of multiple disorders: The medas system,” *IEEE Trans. Pattern Anal. Mach. Intell.*, vol. PAMI-2, no. 2, pp. 148–160, 1980.
- [8] Y. Pan *et al.*, “Disease-image-specific learning for diagnosis-oriented neuroimage synthesis with incomplete multi-modality data,” *IEEE Trans. Pattern Anal. Mach. Intell.*, vol. 44, no. 10, pp. 6839–6853, 2022.
- [9] G. Pu *et al.*, “Controllable image synthesis with attribute-decomposed gan,” *IEEE Trans. Pattern Anal. Mach. Intell.*, vol. 45, no. 2, pp. 1514–1532, 2023.
- [10] C. R. Green *et al.*, “Functional decline in alzheimer’s disease: a longitudinal study,” *Journal of the American Geriatrics Society*, vol. 41, no. 6, pp. 654–661, 1993.
- [11] D. K. Johnson *et al.*, “Longitudinal study of the transition from healthy aging to alzheimer disease,” *Archives of neurology*, vol. 66, no. 10, pp. 1254–1259, 2009.
- [12] E. McDade *et al.*, “Longitudinal cognitive and biomarker changes in dominantly inherited alzheimer disease,” *Neurology*, vol. 91, no. 14, pp. e1295–e1306, 2018.
- [13] T. Karras *et al.*, “A style-based generator architecture for generative adversarial networks,” in *IEEE/CVF CVPR*, pp. 4401–4410, 2019.
- [14] S. Hong *et al.*, “3d-stylegan: A style-based generative adversarial network for generative modeling of three-dimensional medical images,” in *Deep Generative Models, and Data Augmentation, Labelling, and Imperfections: First Workshop, DGM4MICCAI 2021, and First Workshop, DALI 2021, Held in Conjunction with MICCAI 2021, Strasbourg, France, October 1, 2021, Proceedings 1*, pp. 24–34, Springer, 2021.
- [15] T. Karras *et al.*, “Analyzing and improving the image quality of stylegan,” in *IEEE/CVF CVPR*, pp. 8110–8119, 2020.
- [16] E. Richardson *et al.*, “Encoding in style: a stylegan encoder for image-to-image translation,” in *IEEE/CVF CVPR*, pp. 2287–2296, 2021.
- [17] O. Tov *et al.*, “Designing an encoder for stylegan image manipulation,” *ACM Transactions on Graphics (TOG)*, vol. 40, no. 4, pp. 1–14, 2021.
- [18] J. Pearl, *Causality*. Cambridge University Press, 2 ed., 2009.
- [19] Y. Liu *et al.*, “Learning temporal causal graphs for relational time-series analysis,” in *ICML*, pp. 687–694, 2010.
- [20] M. Parascandola *et al.*, “Causation in epidemiology,” *Journal of Epidemiology & Community Health*, vol. 55, no. 12, pp. 905–912, 2001.
- [21] H. Wold, “Causality and econometrics,” *Econometrica: Journal of the Econometric Society*, pp. 162–177, 1954.
- [22] B. Kuipers *et al.*, “Causal reasoning in medicine: analysis of a protocol,” *Cognitive Science*, vol. 8, no. 4, pp. 363–385, 1984.
- [23] N. Pawlowski *et al.*, “Deep structural causal models for tractable counterfactual inference,” *Proc. Adv. Neural Inf. Process. Syst.*, vol. 33, pp. 857–869, 2020.
- [24] C. K. Assaad *et al.*, “Survey and evaluation of causal discovery methods for time series,” *Journal of Artificial Intelligence Research*, vol. 73, pp. 767–819, 2022.
- [25] P. S. Aisen *et al.*, “Clinical core of the alzheimer’s disease neuroimaging initiative: progress and plans,” *Alzheimer’s & Dementia*, vol. 6, no. 3, pp. 239–246, 2010.

- [26] D. L. Beekly *et al.*, "The national alzheimer's coordinating center (nacc) database: the uniform data set," *Alzheimer Disease & Associated Disorders*, vol. 21, no. 3, pp. 249–258, 2007.
- [27] P. J. LaMontagne *et al.*, "Oasis-3: longitudinal neuroimaging, clinical, and cognitive dataset for normal aging and alzheimer disease," *MedRxiv*, pp. 2019–12, 2019.
- [28] D. P. Kingma and M. Welling, "Auto-encoding variational bayes," *arXiv preprint arXiv:1312.6114*, 2013.
- [29] O. Ronneberger *et al.*, "U-net: Convolutional networks for biomedical image segmentation," in *MICCAI*, pp. 234–241, Springer, 2015.
- [30] I. Goodfellow *et al.*, "Generative adversarial networks," *Communications of the ACM*, vol. 63, no. 11, pp. 139–144, 2020.
- [31] J. Ho *et al.*, "Denosing diffusion probabilistic models," *Proc. Adv. Neural Inf. Process. Syst.*, vol. 33, pp. 6840–6851, 2020.
- [32] C. F. Baumgartner *et al.*, "Visual feature attribution using wasserstein gans," in *IEEE/CVF CVPR*, pp. 8309–8319, 2018.
- [33] S. Momeni *et al.*, "Generative model of brain microbleeds for mri detection of vascular marker of neurodegenerative diseases," *Frontiers in Neuroscience*, vol. 15, p. 778767, 2021.
- [34] S. Momeni *et al.*, "Generative model of brain microbleeds for mri detection of vascular marker of neurodegenerative diseases," *Frontiers in Neuroscience*, vol. 15, p. 778767, 2021.
- [35] J. M. Edmund *et al.*, "A review of substitute ct generation for mri-only radiation therapy," *Radiation Oncology*, vol. 12, pp. 1–15, 2017.
- [36] V. M. H. Phan *et al.*, "Structure-preserving synthesis: Maskgan for unpaired mr-ct translation," in *MICCAI*, pp. 56–65, Springer, 2023.
- [37] W. Lin *et al.*, "Bidirectional mapping of brain mri and pet with 3d reversible gan for the diagnosis of alzheimer's disease," *Frontiers in Neuroscience*, vol. 15, p. 646013, 2021.
- [38] S. Hu *et al.*, "Bidirectional mapping generative adversarial networks for brain mr to pet synthesis," *IEEE Trans. Med. Imag.*, vol. 41, no. 1, pp. 145–157, 2022.
- [39] Y. Pan *et al.*, "Disease-image specific generative adversarial network for brain disease diagnosis with incomplete multi-modal neuroimages," in *MICCAI*, pp. 137–145, Springer, 2019.
- [40] Y. Wang *et al.*, "3d auto-context-based locality adaptive multi-modality gans for pet synthesis," *IEEE Trans. Med. Imag.*, vol. 38, no. 6, pp. 1328–1339, 2019.
- [41] Y. Li *et al.*, "A review of the deep learning methods for medical images super resolution problems," *Irbm*, vol. 42, no. 2, pp. 120–133, 2021.
- [42] S. U. Dar *et al.*, "Image synthesis in multi-contrast mri with conditional generative adversarial networks," *IEEE Trans. Med. Imag.*, vol. 38, no. 10, pp. 2375–2388, 2019.
- [43] Y. Zhang *et al.*, "Unified multi-modal image synthesis for missing modality imputation," *arXiv preprint arXiv:2304.05340*, 2023.
- [44] C. Fan *et al.*, "Tr-gan: Multi-session future mri prediction with temporal recurrent generative adversarial network," *IEEE Trans. Med. Imag.*, vol. 41, no. 8, pp. 1925–1937, 2022.
- [45] Y. Zhao *et al.*, "Prediction of alzheimer's disease progression with multi-information generative adversarial network," *IEEE J. Biomed. Health Inform.*, vol. 25, no. 3, pp. 711–719, 2020.
- [46] Z. Ning *et al.*, "Ldgan: Longitudinal-diagnostic generative adversarial network for disease progression prediction with missing structural mri," in *MLMI*, pp. 170–179, Springer, 2020.
- [47] J. C. Reinhold *et al.*, "A structural causal model for mr images of multiple sclerosis," in *MICCAI*, pp. 782–792, Springer, 2021.
- [48] A. Kumar *et al.*, "Counterfactual image synthesis for discovery of personalized predictive image markers," in *MICCAI Workshop on Medical Image Assisted Biomarkers' Discovery*, pp. 113–124, Springer, 2022.
- [49] P. Sanchez *et al.*, "What is healthy? generative counterfactual diffusion for lesion localization," in *MICCAI Workshop on Deep Generative Models*, pp. 34–44, Springer, 2022.
- [50] C. L. Van Broeckhoven, "Molecular genetics of alzheimer disease: identification of genes and gene mutations," *European neurology*, vol. 35, no. 1, pp. 8–19, 1995.
- [51] E. Levy-Lahad *et al.*, "Candidate gene for the chromosome 1 familial alzheimer's disease locus," *Science*, vol. 269, no. 5226, pp. 973–977, 1995.
- [52] N. D. Beckmann *et al.*, "Multiscale causal networks identify vgf as a key regulator of alzheimer's disease," *Nature communications*, vol. 11, no. 1, p. 3942, 2020.
- [53] T. L. Spire-Jones *et al.*, "The intersection of amyloid beta and tau at synapses in alzheimer's disease," *Neuron*, vol. 82, no. 4, pp. 756–771, 2014.
- [54] H.-C. Huang *et al.*, "Accumulated amyloid- $\beta$  peptide and hyperphosphorylated tau protein: relationship and links in alzheimer's disease," *Journal of Alzheimer's disease*, vol. 16, no. 1, pp. 15–27, 2009.
- [55] R. Rajmohan *et al.*, "Amyloid-beta and phosphorylated tau accumulations cause abnormalities at synapses of alzheimer's disease neurons," *Journal of Alzheimer's Disease*, vol. 57, no. 4, pp. 975–999, 2017.
- [56] P. H. Reddy *et al.*, "Amyloid beta and phosphorylated tau-induced defective autophagy and mitophagy in alzheimer's disease," *Cells*, vol. 8, no. 5, p. 488, 2019.
- [57] P. A. Thomann *et al.*, "Association of total tau and phosphorylated tau 181 protein levels in cerebrospinal fluid with cerebral atrophy in mild cognitive impairment and alzheimer disease," *Journal of Psychiatry and Neuroscience*, vol. 34, no. 2, pp. 136–142, 2009.
- [58] W. Pelkmans *et al.*, "Tau-related grey matter network breakdown across the alzheimer's disease continuum," *Alzheimer's Research & Therapy*, vol. 13, pp. 1–11, 2021.
- [59] A. Bejanin *et al.*, "Tau pathology and neurodegeneration contribute to cognitive impairment in alzheimer's disease," *Brain*, vol. 140, no. 12, pp. 3286–3300, 2017.
- [60] V. Kasantikul *et al.*, "Relation of age and cerebral ventricle size to central canal in man: Morphological analysis," *Journal of neurosurgery*, vol. 51, no. 1, pp. 85–93, 1979.
- [61] K. Skullerud, "Variations in the size of the human brain. influence of age, sex, body length, body mass index, alcoholism, alzheimer changes, and cerebral atherosclerosis," *Acta neurologica Scandinavica. Supplementum*, vol. 102, pp. 1–94, 1985.
- [62] M. P. Earnest *et al.*, "Cortical atrophy, ventricular enlargement and intellectual impairment in the aged," *Neurology*, vol. 29, no. 8, pp. 1138–1138, 1979.
- [63] C. A. Raji *et al.*, "Age, alzheimer disease, and brain structure," *Neurology*, vol. 73, no. 22, pp. 1899–1905, 2009.
- [64] R. Guerreiro *et al.*, "The age factor in alzheimer's disease," *Genome medicine*, vol. 7, no. 1, pp. 1–3, 2015.
- [65] C. Kawas *et al.*, "Age-specific incidence rates of alzheimer's disease: the baltimore longitudinal study of aging," *Neurology*, vol. 54, no. 11, pp. 2072–2077, 2000.
- [66] Y. Stern *et al.*, "Influence of education and occupation on the incidence of alzheimer's disease," *Jama*, vol. 271, no. 13, pp. 1004–1010, 1994.
- [67] M. Paradise *et al.*, "Systematic review of the effect of education on survival in alzheimer's disease," *International psychogeriatrics*, vol. 21, no. 1, pp. 25–32, 2009.
- [68] C. M. Mazure *et al.*, "Sex differences in alzheimer's disease and other dementias," *The Lancet Neurology*, vol. 15, no. 5, pp. 451–452, 2016.
- [69] R. Li *et al.*, "Sex differences in cognitive impairment and alzheimer's disease," *Frontiers in neuroendocrinology*, vol. 35, no. 3, pp. 385–403, 2014.
- [70] L. Guo *et al.*, "Sex differences in alzheimer's disease: Insights from the multiomics landscape," *Biological psychiatry*, vol. 91, no. 1, pp. 61–71, 2022.
- [71] G. Karas *et al.*, "Global and local gray matter loss in mild cognitive impairment and alzheimer's disease," *Neuroimage*, vol. 23, no. 2, pp. 708–716, 2004.
- [72] G. Karas *et al.*, "A comprehensive study of gray matter loss in patients with alzheimer's disease using optimized voxel-based morphometry," *Neuroimage*, vol. 18, no. 4, pp. 895–907, 2003.
- [73] S. A. Rombouts *et al.*, "Unbiased whole-brain analysis of gray matter loss in alzheimer's disease," *Neuroscience letters*, vol. 285, no. 3, pp. 231–233, 2000.
- [74] L. Ferrarini *et al.*, "Shape differences of the brain ventricles in alzheimer's disease," *Neuroimage*, vol. 32, no. 3, pp. 1060–1069, 2006.
- [75] P. M. Thompson *et al.*, "Mapping hippocampal and ventricular change in alzheimer disease," *Neuroimage*, vol. 22, no. 4, pp. 1754–1766, 2004.
- [76] Y.-Y. Chou *et al.*, "Mapping correlations between ventricular expansion and csf amyloid and tau biomarkers in 240 subjects with alzheimer's disease, mild cognitive impairment and elderly controls," *Neuroimage*, vol. 46, no. 2, pp. 394–410, 2009.

- [77] M. De Leon *et al.*, "Longitudinal cerebrospinal fluid tau load increases in mild cognitive impairment," *Neuroscience letters*, vol. 333, no. 3, pp. 183–186, 2002.
- [78] L. Letenneur, V. Gilleron, *et al.*, "Are sex and educational level independent predictors of dementia and alzheimer's disease? incidence data from the paquid project," *Journal of Neurology, Neurosurgery & Psychiatry*, vol. 66, no. 2, pp. 177–183, 1999.
- [79] L. Fratiglioni *et al.*, "Prevalence of alzheimer's disease and other dementias in an elderly urban population: relationship with age, sex, and education," *Neurology*, vol. 41, no. 12, pp. 1886–1886, 1991.
- [80] B. C. Riedel *et al.*, "Age, apoe and sex: triad of risk of alzheimer's disease," *The Journal of steroid biochemistry and molecular biology*, vol. 160, pp. 134–147, 2016.
- [81] R. Mayeux *et al.*, "Plasma  $\alpha$ 40 and  $\alpha$ 42 and alzheimer's disease: relation to age, mortality, and risk," *Neurology*, vol. 61, no. 9, pp. 1185–1190, 2003.
- [82] E. Dicks *et al.*, "Modeling grey matter atrophy as a function of time, aging or cognitive decline show different anatomical patterns in alzheimer's disease," *NeuroImage: Clinical*, vol. 22, p. 101786, 2019.
- [83] Y.-Y. Chou *et al.*, "Mapping correlations between ventricular expansion and csf amyloid and tau biomarkers in 240 subjects with alzheimer's disease, mild cognitive impairment and elderly controls," *Neuroimage*, vol. 46, no. 2, pp. 394–410, 2009.
- [84] N. Villain *et al.*, "Sequential relationships between grey matter and white matter atrophy and brain metabolic abnormalities in early alzheimer's disease," *Brain*, vol. 133, no. 11, pp. 3301–3314, 2010.
- [85] S. A. Mulaik, *Linear causal modeling with structural equations*. CRC press, 2009.
- [86] G. Zhao *et al.*, "Diagnose like a radiologist: Hybrid neuro-probabilistic reasoning for attribute-based medical image diagnosis," *IEEE Trans. Pattern Anal. Mach. Intell.*, vol. 44, no. 11, pp. 7400–7416, 2021.
- [87] X. Shen *et al.*, "Challenges and opportunities with causal discovery algorithms: application to alzheimer's pathophysiology," *Scientific reports*, vol. 10, no. 1, p. 2975, 2020.
- [88] Y. Iturria-Medina *et al.*, "Multifactorial causal model of brain (dis) organization and therapeutic intervention: Application to alzheimer's disease," *Neuroimage*, vol. 152, pp. 60–77, 2017.
- [89] Y. Iturria-Medina *et al.*, "Early role of vascular dysregulation on late-onset alzheimer's disease based on multifactorial data-driven analysis," *Nature communications*, vol. 7, no. 1, p. 11934, 2016.
- [90] C. R. Jack *et al.*, "Tracking pathophysiological processes in alzheimer's disease: an updated hypothetical model of dynamic biomarkers," *The lancet neurology*, vol. 12, no. 2, pp. 207–216, 2013.
- [91] M. C. Donohue *et al.*, "Estimating long-term multivariate progression from short-term data," *Alzheimer's & Dementia*, vol. 10, pp. S400–S410, 2014.
- [92] J. Jia *et al.*, "Biomarker changes during 20 years preceding alzheimer's disease," *New England Journal of Medicine*, vol. 390, no. 8, pp. 712–722, 2024.
- [93] A. Abdulaal *et al.*, "Deep structural causal modelling of the clinical and radiological phenotype of alzheimer's disease," in *NeurIPS 2022 Workshop on Causality for Real-world Impact*, 2022.
- [94] H. Hu *et al.*, "Improved causal models of alzheimer's disease," in *2021 IEEE 45th Annual Computers, Software, and Applications Conference (COMPSAC)*, pp. 274–283, 2021.
- [95] R. V. Marinescu *et al.*, "Tadpole challenge: prediction of longitudinal evolution in alzheimer's disease," *arXiv preprint arXiv:1805.03909*, 2018.
- [96] R. V. Marinescu *et al.*, "The alzheimer's disease prediction of longitudinal evolution (tadpole) challenge: Results after 1 year follow-up," *arXiv preprint arXiv:2002.03419*, 2020.
- [97] Y. Utsumil *et al.*, "Personalized gaussian processes for forecasting of alzheimer's disease assessment scale-cognition subscale (adas-cog13)," in *2018 40th Annual International Conference of the IEEE Engineering in Medicine and Biology Society (EMBC)*, pp. 4007–4011, IEEE, 2018.
- [98] C. Sevilla-Salcedo *et al.*, "Multi-task longitudinal forecasting with missing values on alzheimer's disease," *Computer Methods and Programs in Biomedicine*, vol. 226, p. 107056, 2022.
- [99] M. M. Ghazi *et al.*, "Robust parametric modeling of alzheimer's disease progression," *NeuroImage*, vol. 225, p. 117460, 2021.
- [100] M. Nguyen *et al.*, "Predicting alzheimer's disease progression using deep recurrent neural networks," *NeuroImage*, vol. 222, p. 117203, 2020.
- [101] S. Hochreiter *et al.*, "Long short-term memory," *Neural Comput.*, vol. 9, no. 8, pp. 1735–1780, 1997.
- [102] C. Durkan *et al.*, "Neural spline flows," *Proc. Adv. Neural Inf. Process. Syst.*, vol. 32, 2019.
- [103] P. L. Spirtes *et al.*, "Causal inference in the presence of latent variables and selection bias," *arXiv preprint arXiv:1302.4983*, 2013.
- [104] D. M. Chickering, "Optimal structure identification with greedy search," *Journal of machine learning research*, vol. 3, no. Nov, pp. 507–554, 2002.
- [105] S. Shimizu *et al.*, "Directlingam: A direct method for learning a linear non-gaussian structural equation model," *Journal of Machine Learning Research*, vol. 12, no. Apr, pp. 1225–1248, 2011.
- [106] J. E. Iglesias *et al.*, "Robust brain extraction across datasets and comparison with publicly available methods," *IEEE Trans. Med. Imag.*, vol. 30, no. 9, pp. 1617–1634, 2011.
- [107] B. B. Avants *et al.*, "Advanced normalization tools (ants)," *Insight j*, vol. 2, no. 365, pp. 1–35, 2009.
- [108] M. Shao *et al.*, "Brain ventricle parcellation using a deep neural network: Application to patients with ventriculomegaly," *NeuroImage: Clinical*, vol. 23, p. 101871, 2019.
- [109] W. H. Pinaya *et al.*, "Brain imaging generation with latent diffusion models," in *MICCAI Workshop on Deep Generative Models*, pp. 117–126, Springer, 2022.
- [110] W. H. Pinaya *et al.*, "Generative ai for medical imaging: extending the monai framework," *arXiv preprint arXiv:2307.15208*, 2023.
- [111] C. Sudlow *et al.*, "Uk biobank: an open access resource for identifying the causes of a wide range of complex diseases of middle and old age," *PLoS medicine*, vol. 12, no. 3, p. e1001779, 2015.
- [112] A. B. L. Larsen *et al.*, "Autoencoding beyond pixels using a learned similarity metric," in *ICML*, pp. 1558–1566, PMLR, 2016.
- [113] I. Gulrajani *et al.*, "Improved training of wasserstein gans," *Proc. Adv. Neural Inf. Process. Syst.*, vol. 30, 2017.
- [114] L. Sun *et al.*, "Hierarchical amortized gan for 3d high resolution medical image synthesis," *IEEE journal of biomedical and health informatics*, vol. 26, no. 8, pp. 3966–3975, 2022.
- [115] P. Isola *et al.*, "Image-to-image translation with conditional adversarial networks," in *IEEE/CVF CVPR*, pp. 1125–1134, 2017.
- [116] J.-Y. Zhu *et al.*, "Unpaired image-to-image translation using cycle-consistent adversarial networks," in *IEEE/CVF CVPR*, pp. 2223–2232, 2017.



**Yujia Li** received the B.E. degree from Tsinghua University in 2021. She is currently pursuing the Ph.D. degree from the and the M.S. degree in computer science from the Institute of Computing Technology (ICT), University of Chinese Academy of Sciences (UCAS). Her research interests include computer vision, machine learning and image processing, with applications to biomedical engineering.



**Han Li** received the B.E. degree from Henan Polytechnic University (HPU) in 2016, and the M.S. degree in computer science from the Institute of Computing Technology (ICT), University of Chinese Academy of Sciences (UCAS) in 2021. He is currently pursuing the Ph.D. degree from the School of Biomedical Engineering & Suzhou Institute for Advanced Research, University of Science and Technology of China (USTC). His research interests include computer vision, machine learning and image processing,

with applications to biomedical engineering.



**Prof. S. Kevin Zhou** (Fellow, IEEE) obtained his Ph.D degree from the University of Maryland, College Park. Currently, he is a distinguished professor and founding executive dean of the School of Biomedical Engineering, Suzhou Institute for Advanced Research, University of Science and Technology of China (USTC), and an adjunct professor at the Institute of Computing Technology, Chinese Academy of Sciences. He directs the Center for Medical Imaging, Robotics, Analytic Computing and Learning (MIRACLE).

Prior to this, he was a principal expert and a senior R&D director at Siemens Healthcare Research. Dr. Zhou has published 260+ book chapters and peer-reviewed journal and conference papers, registered 140+ granted patents, written three research monographs, and edited three books. The most recent book he led the edition is entitled "Handbook of Medical Image Computing and Computer Assisted Intervention, SK Zhou, D Rueckert, G Fichtinger (Eds.)" and the book he coauthored most recently is entitled "Deep Network Design for Medical Image Computing, H Liao, SK Zhou, J Luo". He has won multiple awards including R&D 100 Award (Oscar of Invention), Siemens Inventor of the Year, UMD ECE Distinguished Alumni Award, BMEF Editor of the Year, and Finalist Paper for MICCAI Young Scientist Award (twice). He has been a program co-chair for MICCAI2020, and an associate editor for IEEE Trans. Medical Imaging, IEEE Trans. Pattern Analysis Machine Intelligence, Medical Image Analysis, and an area chair for AAAI, CVPR, ICCV, MICCAI, and NeurIPS. He has been elected as a treasurer and board member of the MICCAI Society, an advisory board member of MONAI (Medical Open Network for AI), and a fellow of AIMBE, IAMBE, IEEE, MICCAI, and NAI.